CHALMERS

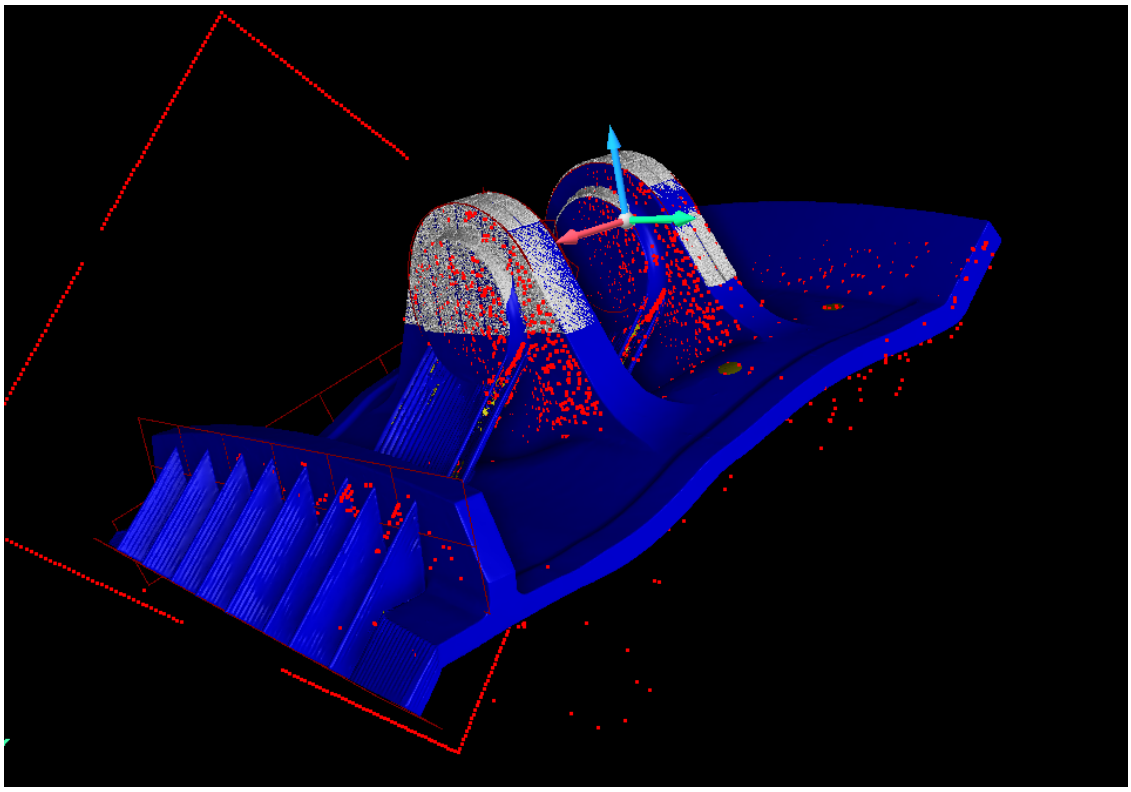

Capability determination of in-process monitoring for laser powder bed fusion

A study on the detection and correlation of spatter-induced defects using optical tomography and XCT

Master's thesis in Production Engineering

Philip Dynevik
Nils Severinson

Department of Industrial- and Materials Science

CHALMERS UNIVERSITY OF TECHNOLOGY
Gothenburg 2025
www.chalmers.se

Master's Thesis 2025

Capability determination of in-process monitoring for laser powder bed fusion

A study on the detection and correlation of spatter-induced defects using optical tomography and XCT

PHILIP DYNEVIK
NILS SEVERINSON

CHALMERS

Department of Industrial- and Materials Science
Chalmers University of Technology
Gothenburg, Sweden 2025

Capability determination of in-process monitoring for laser powder bed fusion
A study on the detection and correlation of spatter-induced defects using optical tomography and XCT
PHILIP DYNEVIK
NILS SEVERINSON

Supervisor: Mats Delin, GKN Aerospace
Arda Baytaroglu, GKN Aerospace
Lars Nyborg, Industrial- and Materials Science
Examiner: Lars Nyborg, Industrial- and Materials Science

Master's Thesis 2025
Department of Industrial- and Materials Science
Chalmers University of Technology
SE-412 96 Gothenburg
Telefon +46 31 772 1000

Cover: Visualization of the GOM scan of the demonstrator (in blue) aligned with the XCT-scanned mounts, along with the generated OT point cloud, all rendered in Volume Graphics.

Typeset in LaTeX
Printed by Chalmers Reproservice
Gothenburg 2025

Capability determination of in-process monitoring for laser powder bed fusion
A study on the detection and correlation of spatter-induced defects using optical tomography and XCT
PHILIP DYNEVIK
NILS SEVERINSON
Department of Industrial- and Materials Science
Chalmers University of Technology

Abstract

This thesis investigates the capability of optical tomography (OT) as an in-situ process monitoring tool for detecting spatter-induced defects in components produced via Laser Powder Bed Fusion (LPBF). The study evaluates whether OT imaging, combined with custom image processing techniques, can reliably identify internal porosities typically verified through high-resolution X-ray Computed Tomography (XCT).

Two Inconel 718 demonstrator parts were manufactured using an EOS M290 LPBF machine, with process parameters deliberately adjusted to promote defect formation. OT images captured during the build were processed using a custom MATLAB script that applied Laplacian of Gaussian (LoG) and erosion filtering to identify thermal anomalies. These anomalies were compiled into point cloud datasets and digitally compared with XCT data of the segmented demonstrator.

The results revealed limited correlation between OT-based indications and actual porosities detected through XCT, with alignment errors, image noise, and the resolution of OT data identified as key limitations. Despite this, the study highlights spatial patterns in OT data that may still be indicative of defect-prone regions, suggesting potential for further development. The findings underscore the need for enhanced filtering techniques, improved data alignment, and the integration of additional OT data types to improve detection accuracy.

This work contributes to the ongoing development of in-situ monitoring systems for LPBF, particularly in critical applications like aerospace, where early defect detection is vital for part certification and safety assurance.

Keywords: Laser Powder Bed Fusion, Optical Tomography, In-situ Monitoring, X-ray Computed Tomography, Defect Detection, Spatter, Inconel 718.

Acknowledgements

We would like to express our deepest gratitude to our supervisors Arda Baytaroglu and Mats Delin at GKN Aerospace for their invaluable support throughout this thesis. Arda, thank you for your continuous dedication, availability, and hands-on guidance, your daily support made a real difference in our work. Mats, your experience and extensive network were instrumental in shaping the direction of our project, and we are truly grateful for your Support.

We would also like to thank our academic supervisor, Professor Lars Nyborg at Chalmers University of Technology, for his expert guidance and deep knowledge in the field. His feedback and insights were critical in helping us navigate each step of the research process.

Finally, a warm thank you to the entire Materials and Inspection team at GKN Aerospace for welcoming us from day one and creating an open, supportive environment throughout our time with the company.

Thank you all for making this project both insightful and enjoyable.

Philip Dynevik, Gothenburg, June 2025
Nils Severinson, Gothenburg, June 2025

Disclosure for the use of AI-tools for thesis report writing

This thesis has been written with the support of various AI tools to improve the overall quality and efficiency of the work. These tools were used to improve sentence structure, propose support for clarity and flow of the text, assist with grammar and spelling, and support in parts of the coding process. All core ideas, analysis, interpretations, and conclusions presented in this thesis were entirely developed by the authors.

AI-tools used:

- ChatGPT: Utilized to enhance sentence structure, improve the flow of the text, and support clarity in written communication
- Copilot: Used as a coding assistant during the development of custom scripts, providing suggestions for syntax, logic, and function structure.

Acronyms

Below is the list of acronyms that have been used throughout this thesis listed in alphabetical order:

AM	Additive Manufacturing
AWJ	Abrasive Water Jet
CAD	Computer-Aided Design
CNN	Convolutional Neural Network
EDM	Electrical Discharge Machining
EOS	Electro Optical Systems (refers to EOS M290 machine)
GOM	Geometric Object Modeling (3D scanning system)
LPBF	Laser Powder Bed Fusion
OT	Optical Tomography
PBF	Powder Bed Fusion
SLM	Selective Laser Melting
TIFF	Tagged Image File Format
VGS	shorthand for VGSTUDIO
XCT	X-ray Computed Tomography

Nomenclature

Below is the nomenclature of symbols and variables used throughout this thesis, based on optical tomography, image filtering, and XCT analysis.

Variables

$f(x, y)$	Pixel intensity at coordinates (x, y) in the OT image
$G(x, y; \sigma)$	Gaussian smoothing function
$\nabla^2 f$	Laplacian of the image intensity function (second-order derivative)

Contents

List of Figures

List of Tables

1

Introduction

1.1 Background to Project

In recent years, additive manufacturing (AM) has emerged as one of the most versatile production processes, offering unparalleled design freedom. This capability enables greater customization of components, adding significant value, particularly in applications such as medical implants and aerospace components [1].

Among metal additive manufacturing technologies, there are various processes in which Powder Bed Fusion (PBF) is the most widely used and well-established [1] [2]. Mostly because of its low manufacturing cost and the ability to recycle the powder used to manufacture a new component. This process builds components layer by layer, allowing for geometries with complex internal cavities that would be difficult or nearly impossible to achieve with conventional manufacturing methods. The PBF process can be utilized using a laser or an electron beam, where Laser Powder Bed Fusion (LPBF) is the most common one [2].

Although additive manufacturing offers significant potential, several challenges persist, particularly in quality control and process validation, which remain costly and complex. One of the biggest challenges in LPBF is the selection of optimized process parameters for effective production while still maintaining favorable structural properties [3]. Insufficient parameter selection can lead to the formation of unfavorable defects or long print times that negatively impact lead times. Even when optimal parameters are chosen, defects may still occur due to stochastic spatter or trapped gas pores [3]. These deviations can increase the porosity of the component produced, making it more difficult to verify the quality and durability of the final product. As a result, the ability to predict and mitigate these defects in real-time is crucial to advance LPBF technology and its application in demanding industries such as aerospace.

GKN Aerospace, a global leader in aerospace development, supplies components for the majority of today's commercial and defense aircrafts [4]. Given the high quality standards of the aerospace sector and its need to remain competitive, there is a continuous drive to adopt the most efficient manufacturing methods available [5]. Metal additive manufacturing is currently regarded as a leading contender in achieving this goal, offering potential improvements in both the efficiency and cost-effectiveness of manufacturing.

This thesis project explores the potential for in-situ monitoring of the LPBF process in the production of an airplane engine mount at GKN Aerospace. Using process monitoring data, this study aims to assess whether it is possible to predict defects or whether additional validation methods, such as post-process inspections or computational models, are required. The objective is to provide valuable information on the feasibility of using real-time process data for defect detection and quality control in aerospace manufacturing.

The engine mount is made from Inconel 718, which is a superalloy known for its mechanical properties and weldability and is therefore often used in aerospace applications [6]. The mount consists of one base with two elevated sections that are all manufactured using the LPBF process (see Figure 1.1). Understanding and ensuring the quality of these types of parts is vital, as any defect could compromise safety and performance.

(a) Demonstrator side view **(b)** Demonstrator side view

Figure 1.1: The engine mount.

The surface geometry of the engine mount is captured using Geometric Object Modeling (GOM), which is used to scan the surface of the component for irregularities or deviations in shape or surface finish compared to the CAD model. After construction, the mount has also been stress relieved using heat treatment.

1.2 Problem statement

The demonstrator being investigated, an aircraft engine mount, is a component that requires high durability and the ability to perform under high temperatures. These

demands make the choice of material crucial and are the reason why the Inconel 718 alloy was chosen. During the LPBF process, defects can occur that in turn can lead to an increased risk of cracks and reduced durability. This can occur for various reasons and includes the lack of fusion, porosities, or surface imperfections [7], which will weaken the material and its properties at certain points. Another big contributor is stochastic spatter, which can manifest in the powder bed and cause the defects mentioned above. In recent years, optical tomography (OT) has gained attention as a potential in-situ monitoring method. However, there is limited evidence showing that OT data alone can accurately detect internal porosities, especially when compared to XCT validation.

1.3 Research questions & objectives

The following research questions will be used for this thesis.

1. How accurately can OT images detect spatter induced defects during the powder bed fusion process?

2. What are the limitations of using OT-based image processing for detecting internal porosities in LPBF, and how can these be addressed?

1.4 Scope & Limitations

To ensure that the master thesis remains within the scope of the project, some limitations have been set. According to Chalmers regulations, this master's thesis project is limited to one semester, which is 20 weeks of full-time studies. This is approximately 800 hours per person and will be conducted between the 15th of January and the 6th of June.

This master's thesis is limited to investigate and focus on the validation of in-process monitoring to detect defects during laser powder bed fusion processes. More specifically, defects related to stochastic spatter. For the project, materials and manufacturing processes were also predetermined, specifically two Inconel 718 demonstrators produced using an EOS M290 LPBF machine. The project will also rely on precollected OT data from the manufacturing of the two demonstrators.

Several challenges and areas are outside the scope of this project. For example, real-time defect correction during the LPBF process is not addressed. Furthermore, this study does not compare the LPBF process with alternative additive manufacturing methods, such as direct energy deposition, which could offer insights into the broader applicability of in-process monitoring. Moreover, the scope is limited to the materials and data currently available, without extending to different alloys or real-time monitoring systems.

2
Technical Background

2.1 Additive Manufacturing

AM, is a process that allows for much freedom in geometry design, such as more complex or customized parts, as there are fewer constraints during the manufacturing process. This is because of the way the process is executed compared to other production methods. AM builds components layer by layer, unlike traditional subtractive manufacturing methods that cut them from a solid block or mold them [8]. This allows for a more material-efficient production, as the produced part generates much less waste than traditional methods. This is because in AM, most of the waste only comes from surface finishing and removal of support structures from the final product. The digital versatility as well as reliability is also notable in AM, the designs for parts are more easily imported directly from digital tools such as CAD models [1], further removing steps that might be present in other processes. It also offers great increases in the production speed of these intricate products [9]. This is in part due to the fact that AM as a single process can in some cases replace multiple processes that would be required to produce the same component. AM is now increasingly accepted and used for the production of high-performance components.

There are a multitude of variants of AM processes that span across many different industries as well as private use, in turn yielding various different applications. In the aerospace and defense industry, it allows the production of lightweight parts that often require complex and hollow geometries, as well as providing opportunities for rapid prototyping [4]. The automotive industry, as broad as it is, benefits for similar reasons, with rapid prototype testing or custom high-performance parts for race cars [10]. In healthcare, AM is already used to make custom prosthetics that require high-durability alloys that are, in turn, not rejected by the body [10].

2.1.1 Metal Additive Manufacturing

As AM has evolved and became more widespread in its implementation areas, so has the desire to use the manufacturing method in additional materials. Metallic components have very favorable mechanical characteristics, as a result, they are also the most common among materials in engineering [9]. As a result, it is natural to have combined the positive production capabilities of AM with the favorable mechanical characteristics that metals bring, resulting in a production method that can rapidly create complex and intricate components with strong mechanical characteristics and little wasted material [9].

2.1.2 Laser Powder Bed Fusion

One of the earliest and first commercially used AM processes was the PBF process [11]. According to Gibson et al. [11] and Chowdury et al. [7] the PBF process is one of the most commonly used processes for AM and can be used with a variety of different materials, such as polymers, metals, ceramics, and composites. The LPBF process is the most common one used for metal AM.

LPBF is a process that includes a laser source, a building platform, a system to deliver powder, a controlling system, and complementary parts such as rollers, scrapers, etc. Where a powder bed is spread out by some type of powder leveling roller on a flat build plate and is then exposed by a high-intensity laser energy through a focus lens and galvano mirrors [7]. The laser is then directed on determined regions to make the desired model shape. This melts the powder, which is then fused layer by layer. When the laser has melted the powder, the build plate is lowered to the desired layer thickness with help of the build piston and the process is repeated when a new layer of powder is spread [1]. After enough iterations, an object is created. The produced object is produced using a CAD 3D model. See Figure 2.1 for visual representation of the LPBF process. Today, the process is limited to a number of different commercial alloy systems, such as, aluminum alloys, titanium alloys, nickel based super alloys or stainless steel [12], while there are numerous more alloys, these are the most commonly used for commercial use. All of which have different properties that can be utilized in different industries.

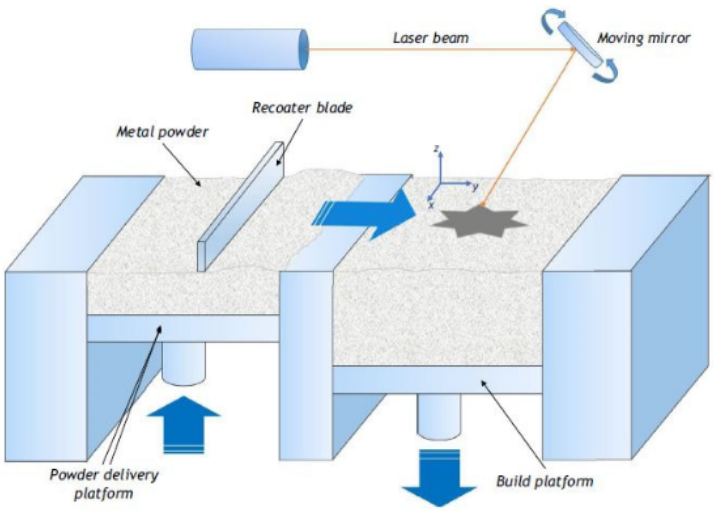

Figure 2.1: Illustration of the LPBF process [13].

The LPBF process offers several notable advantages that make it attractive in modern manufacturing. One of these is its design flexibility. This allows for highly complex and intricate geometries that would be difficult or almost impossible to achieve with traditional methods [7]. Being able to produce these kinds of products has proven beneficial for multiple industries, like aerospace, automotive or medical sectors that often require customized components with strict requirements.

Although the LPBF process offers many benefits, such as a low production time, complex geometries, high material usage and reduced costs [14]. However, challenges remain because the process is dependent on rapid solidification within molten pools of the material leading to the occurrence of thermal stresses, which can result in material segregation and the emergence of non-stable phases. Furthermore, microstructural imperfections such as balling and porosity can be a result of the heat affected zones that occur around the melt pool due to the extensive high heating and cooling rate [7] [14]. These types of defects lead to unwanted properties and reduce the quality of the product. This will be explained in more detail in Section 2.2. By optimizing the process parameters, some defects can be minimized, while others tend to persist. However, this approach is only effective for simple geometries and becomes costly and time-consuming when applied to every new part design.

2.2 Defects in LPBF

As mentioned in section 2.1.2, there are common challenges not yet solved with the LPBF process, and therefore defects in some form are unavoidable. Some of the most common defects in PBF processes include geometric and dimensional inaccuracies, geometrical related defects, surface quality problems, microstructural defects and residual stresses [15] [16] [17]. Moreover, defects arising from spatter and design features also need to be taken into consideration, as they can significantly impact the final part quality and functionality.

2.2.1 Geometrical and dimensional inaccuracies

Geometrical and dimensional inaccuracies originates from deviations in form and size [15] and encompass distortions and deformations such as shrinkage and oversizing [18] [19]. Defects like these influence the structural integrity [20], surface quality and intended use of the part. The low geometric precision is mainly influenced by the staircase effect, errors in machine parameters [15], and thermal stresses [21]. The staircase effect results from the layer-by-layer construction method used in LPBF, where each successive layer introduces stepped edges. This effect becomes particularly pronounced in inclined profiles and in increased layer thickness [22] [23] [24]. According to Druzgalski et al. [25] the LPBF process has more than 130 process parameters that can affect the quality of the final product. These parameters include laser power, velocity, spot size, layer thickness etc. [13] [25] [26]. Thermal stresses arise due to the rapid heating and cooling cycles inherent in the LPBF process, leading to steep thermal gradients and high cooling rates [27]. Moreover, dimensional inaccuracies can lead to super-elevated edges and are influenced by parameters such as building direction, gas flow rate, laser power and scan speed [28].

2.2.2 Geometrical related defects

The design and geometry of the parts produced can significantly influence the occurrence of defects during the process [29]. According to [30] [31] [32] some of the most common defects generated related to geometry include overhang, fine details, and hollow channels.

Overhang structures present a significant challenge in Laser Powder Bed Fusion (LPBF) due to their lack of underlying support. In these regions, the molten metal tends to solidify directly onto the powder bed, which lacks sufficient thermal conductivity and mechanical support. This often leads to issues such as poor surface quality, reduced dimensional accuracy, and incomplete fusion [31], [33]. As a result, parts with large or unsupported overhangs often require redesign or reprinting to meet quality standards.

One of the primary consequences of overhangs is increased warping. Warping occurs when residual stresses, caused by steep temperature gradients during solidification, exceed the material's yield strength and lead to deformation [34]. The severity of warping typically increases with the size of the overhang, especially in the early stages of the construction, when the structure lacks stiffness and thermal conductivity. As the part grows and gains structural support, these effects tend to diminish, but overhangs remain a key factor in warping-related defects.
Fine details in LPBF include smaller parts and thin sections on the part, and share inherent challenges in manufacturing and can have a significant impact on the mechanical properties and structural integrity of manufactured parts. Defects related to fine details often include cracks and distortion due to higher thermal forces on the surface [35], but could also arise due to other factors, such as process parameters or material properties.

Similarly to the other geometrically related defects, hollow channels are also influenced by factors such as process parameters, like laser power or layer thickness, and residual stresses [19]. Common defects in channels and wells produced using LPBF are sag and dross formation [19]. These types of defects can greatly influence the functionality of channels and can be difficult to prevent. A study by Xiaogang et al. [36] showed that channels with a diameter smaller than 2 mm, were unable to remove the remaining powder inside the channels due to shrinkage of the flow channels after fabrication. This leads to post-processing challenges, reduced performance, or contamination of the final part.

2.2.3 Surface quality

The surface quality of the final product can be heavily impacted by surface defects that may occur during the LPBF process. These defects include surface roughness, balling, the staircase effect and spattering [15] [37]. These types of surface defects can affect the mechanical properties, such as the fatigue resistance and corrosion resistance of the final product [22]. Surface roughness is a common defect in LPBF

and could be a result of partially melted surface particles adhering to the surface or incorrect processing parameters [38] [39]. The partially melted particles adhere to the surface because the powder bed is in close contact with the part during solidification, especially on side and downward-facing surfaces. These surfaces experience a higher heat transfer into the surrounding powder, making it easier for loose particles to fuse onto them, resulting in a rougher texture [39].

2.2.4 Microstructural defects

Microstructural defects can significantly affect the structural integrity and properties of parts, often leading to a reduction in tensile strength, increased porosity, and overall structural weaknesses [40] [41]. These defects typically arise from the formation of pores or voids during the manufacturing process. The four primary causes of such defects are Lack of Fusion (LoF), gas pores, keyhole pores, and spatter. Among these, LoF is one of the most prevalent defects in the LPBF process. It occurs when incomplete melting of the powder results in unbonded regions within the material, compromising its mechanical properties and structural integrity [42]. Gas pores can be formed due to the entrapment of gas within the molten pool during rapid solidification of the powder bed, or from LoF porosity caused by the low energy density from the laser[43].

2.2.5 Keyhole pores

Keyhole pores have a spherical shape and are often induced due to high laser power and low scan speeds, which lead to deeper penetration melting [44]. Keyhole pores form when the deep, narrow cavity created by the laser-induced evaporation of metal becomes unstable and collapses. This instability is caused by complex forces that lead to trapped gas pockets that weaken the material [45].

2.2.6 Spatter

Spatter is a common and often unavoidable phenomenon in LPBF. It occurs when the high-energy laser interacts with the metal powder, causing it to melt and sometimes vaporize. Rapid expansion of vapor or recoil pressure from the melt pool leads to hot particles being ejected in various directions. Similarly, cold, unmelted powder particles can also be ejected from the powder bed during the LPBF process. As illustrated in Figure 2.2, the ejection paths of cold and hot particles can differ depending on factors such as the direction of the laser scan and the flow of the gas. While hot particles are typically ejected due to vapor recoil and melt pool dynamics, cold particles are more likely to be displaced by gas flow or mechanical disturbances near the melt pool. These particles, known as spatters, typically range from 25 to 100 µm in size [46]–[48].

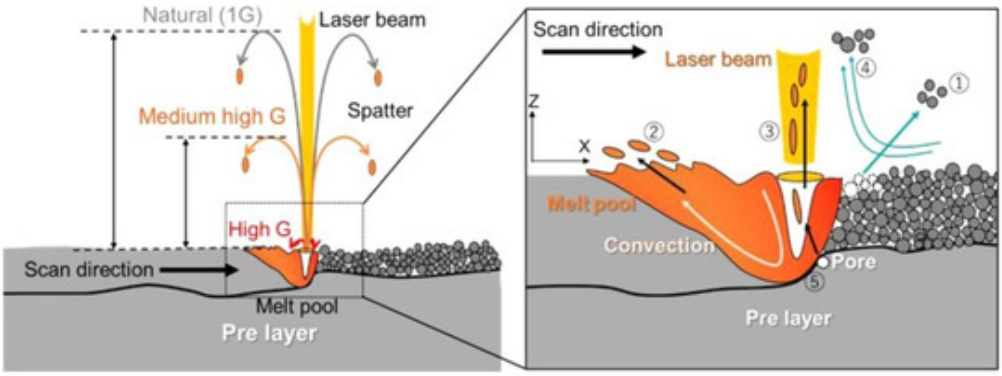

Figure 2.2: Illustration of hot & cold spatter ejection [47].

The behavior and amount of spatter are influenced by several process parameters, such as laser power, scanning speed, and powder properties. For instance, higher laser power or slower scan speeds tend to create larger spatter particles. These particles land back in the melt pool or spread across the powder bed, potentially negatively affecting the building process [49]. Spatter particles can negatively affect both the part that is being built and the powder surrounding it. If the spatter falls back into the melt pool or becomes embedded in new layers, it can lead to defects such as porosity, lack of fusion, and surface roughness [49], [50]. In addition, spatter can contaminate surrounding powder, especially in systems where the powder is reused, reducing the overall quality of future builds [51]. Because spatter forms in unpredictable ways and is difficult to fully control, reducing its impact remains a major focus in process optimization. A better understanding of spatter formation can help improve build quality, powder reusability, and the overall build process [46], [48], [50].

2.2.7 Residual stresses

Residual stresses impose a significant challenge in LPBF, as they can lead to cracks, distortion and delamination [52]. This is often due to rapid melting and solidification in the process, leading to thermal expansion and deformation [52][53]. In the as-built condition, residual stresses vary significantly depending on the surface orientation. On the upper surface, they were approximately half of the material's yield strength, while on the vertically oriented lateral surface, they reached values close to the yield strength. This indicates that the manufacturing process induces substantial internal stresses, particularly in the vertical direction, which can have implications for part performance, dimensional stability, and the need for stress-relief treatments [54][53].

2.3 In-situ Process Monitoring

In-situ process monitoring is a concept that refers to any technology that monitors aspects of a process without interrupting the process flow or destroying the sample [55]. The following section highlights the aspect of process monitoring, more

specifically, it covers the LPBF monitoring process using Optical Tomography. Various aspects can be monitored with regard to LPBF and span between information from both the machine and the processed work object [56]. This section covers the methods that have been used in the production of the samples analyzed in this project.

2.3.1 Optical Tomography (OT)

Since there are a large number of factors that affect the LPBF process, in-situ process monitoring has become essential to keep up with quality standards [57]. One of the primary objectives of in-process monitoring tools is to detect distinct process signatures or indications that can be linked to particular defects or inaccuracies. In this regard, in-situ monitoring tools can identify the early stages of defects during the process, helping minimize material, energy, and time waste. According to Guerra et al. [57] other areas of use include evaluation of geometry and dimensions and detection of defects related to the re-coating system such as elevated edges. Optical tomography (OT) is an imaging technique that utilizes a high resolution camera that captures light radiation from the build process passed through a band-pass filter to capture near infrared wavelengths. This can in turn create images of the entire build surface that capture an object's internal structure by using layer-by-layer imaging [58]. In LPBF, optical tomography monitors the printing process in real time by visualizing how the laser interacts with the powder and melted material. By analyzing pixel intensity values in grayscale images, OT images can be used to identify internal defects such as lack of fusion or spatter [59]. Although OT is effective in detecting spatter-induced defects, the robustness of the processing conditions to spatters can vary, affecting the detection accuracy.

With OT imaging, the monitoring system can generate two types of imaging that can be captured, Integral image or MAX image. The integral image (INT) captures the thermal radiation emitted from the process in the near-infrared wavelength range, integrated over the entire exposure duration. By analyzing the integral image, it becomes possible to observe the average thermal rates across different sections of the part [58]. The MAX image identifies the positions of maximum thermal radiation emitted from the process for a given layer.

2.4 Ex-situ Monitoring

Ex-Situ monitoring is the process of analyzing and measuring parameters outside their original location. Unlike in-situ monitoring, which takes place in the natural environment or during operation, ex-situ monitoring involves collecting data and analyzing them in a controlled environment such as a laboratory [60]. For the sake of this project, the ex-situ monitoring will consist of post-production analysis of the printed demonstrator, in order to compare the result to the result of the in-situ evaluation.

2.4.1 X-ray Computed Tomography

X-ray computed tomography (XCT) is an imaging technique that reconstructs images in a digital form, from measured and collected data that can come from various sources and sensors [61]. X-rays are a form of electromagnetic radiation, like visible light and radio waves. It ranges in wavelengths from 0.01 to 10 nm [62]. Unlike conventional measurement methods, XCT can analyze complex internal and non-line-of-sight surfaces, making it valuable for detecting defects, measuring surface textures and ensuring the quality of components [63]. As XCT is capable of inspecting the internal structure of components, it becomes a very suitable process for metal additively manufactured parts, since they can posses complex geometries hard to analyze with other means of detection [8]. XCT works by firing highly accelerated electrons from a source to a digital detector. Between these two, the element wished to be examined is placed and electrons are fired through the sample towards the detector. Depending on the samples thickness and density, the detector will give different readings [64]. From this firing, the detector can produce a digital 2D projection. Then, the sample is rotated and the process is repeated to produce a multitude of 2D projection that in turn can be compiled to a full 3D reconstruction of the object. The distance from the sample and the intensity of the x-rays also affect the final resolution of the scan. The resolution is defined in voxels. A voxel is a volumetric representation (3D) corresponding to a pixel in two dimensions (2D)[65].

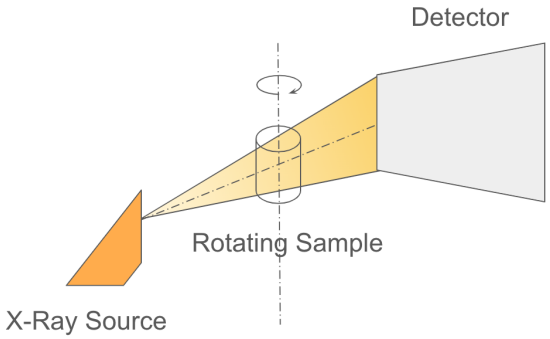

Figure 2.3: XCT Visualization.

The XCT system used for the demonstrator analysis is a Waygate Technologies, Phoenix-Vtomex M240 dual source XCT, which uses an open directional high-power microfocus X-ray tube (240kV), with a closed cooling water circuit. In addition, a open transmission high-power nanofocus X-ray tube (180kV) [66]. The sample is fixed in a rotating 4-axis manipulator, it can be up to 420 mm Ø x 400mm for a 3D scan and weigh up to 50kg (with high-accuracy XCT scans up to approximately 20kg) [66].

2.4.2 Phoenix datos|x - CT Data Acquisition Software

The data produced by the XCT machine is processed in the acquisition software also produced by Waygate Technologies [67]. The software offers the ability to select

which areas of the scan that consists of the work sample and to to reconstruct and export the collected data as a 3D volumetric data for further investigation in other softwares. The phoenix software also offers the ability to investigate these volumes although with limited tools compared to other alternatives. The XCT machine and its interface are directly linked to an external PC that can process its generated data.

2.4.3 VGSTUDIO MAX

VGSTUDIO MAX 2025.1 from Volume Graphics is a software used for geometric, dimensional, and tolerancing analysis, as well as material evaluation, simulation, and XCT reconstruction [68]. It is a widely adopted tool in industry for analyzing and visualizing industrial XCT data. The basic edition includes features such as data quality evaluation, visualization, animation, image segmentation, reporting, and automation [69]. In addition, users can extend the software with more than 20 optional modules customized to specific needs, such as porosity analysis, wall thickness measurement, and volume meshing [68].

One of the features of the software is its quality factor, a numerical scale from 1 to 10, where 1 indicates the lowest quality and 10 the highest. This value reflects the degree of separation between the background and part values, serving as an indicator of clarity and precision in XCT scan porosity analysis.

2.5 Data processing

The vast data available from both in-situ monitoring and process parameters is far too redundant to give defect indications on its own and therefore must be processed to provide insight into the process. The process parameters and values have a great impact on the finished components microstructure and mechanical characteristics of the finished component [70]. With optimal parameters, production time can be kept low while maintaining good mechanical capabilities. Process parameters include laser speed and power, the layer thickness of the powder as well as the printing atmosphere [70]. Correlations can be found between the process parameters and the appearance of defects in the printing process [70]

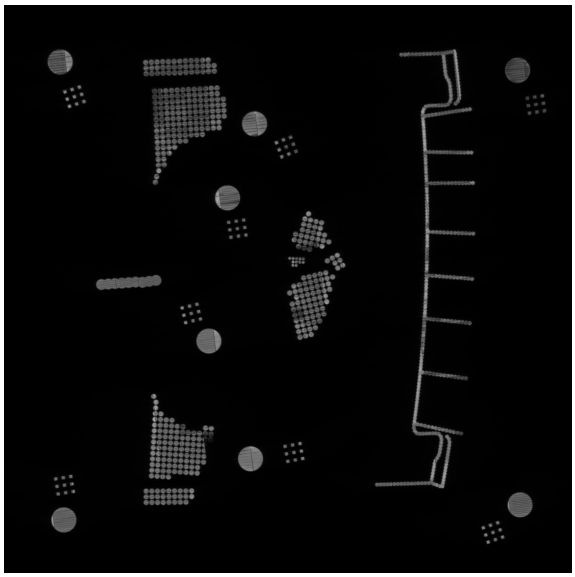

Figure 2.4: Example of an OT image layer

In-situ monitoring data is provided as OT images. The OT data are in the form of MAX OT images, which are black and white 4 megapixel images of the powder bed during the printing of each layer. OT data are the most viable because spatters do not land where the laser points at that moment [71]. In the OT images, the spattered particles manifest as bright spots compared to their surroundings in the image. As spattered particles are shown as bright spots, they can be considered blobs by image processing standards [72]. A blob is a region of an image in which some properties are constant or approximately constant, furthermore, there are methods to recognize these using image processing and recognition software [72].

2.5.1 Laplace of Gaussian and Blob Detection Filters

Of the various different methods for blob detection, the most commonly used one applies a Laplacian of Gaussian (LoG) operator [73]. Other commonly used operators include the Difference of Gaussian (DoG) and Canny edge detection. DoG is one of the first image processing methods, originally used in healthcare before machine learning became more widespread [74]. It works similarly to LoG however, it is just an interpretation of the filter and it does not use a second derivative, thus the computational power required is lower. However, it is not as proficient in edge detection. The Canny edge detection method is also a widely used operator for image processing, and its complexity makes it have many areas of implementation [75]. However, with its complexity comes problems in noise processing, threshold selection and edge selection. For this project, the LoG filter was chosen, as it was seen to have the best characteristics in the sense that it is not to demanding in computational power while at the same time being able to handle sharp image edges.

In a image processing scenario, using an image represented by pixel values:

$$f(x, y) \tag{2.1}$$

Were f is the pixel value represented by x and y coordinates

The Laplace of Gaussian filter applies both the Gaussian function, which smooths out edges between objects displayed in the image:

$$G(x, y; \sigma) = \frac{1}{\sqrt{2\pi\sigma^2}} \exp\left(-\frac{x^2 + y^2}{2\sigma^2}\right) \tag{2.2}$$

Here, sigma is representing a predetermined standard deviation value, normaly around 1

The Laplacian is a second-order differential operator that measures the rate at which the first derivative (gradient) changes. In 2D (for images), it is defined as:

$$\nabla^2 = \frac{\partial^2 f}{\partial x^2} + \frac{\partial^2 f}{\partial y^2} \tag{2.3}$$

A combined representation of the two applied to the before mentioned image [72]:

$$\nabla^2 \mathrm{G}(x, y) = \frac{x^2 + y^2 - 2\sigma^2}{\pi\sigma^4} \exp\left(-\frac{x^2 + y^2}{2\sigma^2}\right) \tag{2.4}$$

The Laplace of Gaussian is used to filter the original image pixel values, it can be used as a method for detecting rapid intensity change in these pixel values [72] [73], in turn, highlighting the local extrema. These extrema in the case of OT data represent a cluster of pixels that are much brighter than their neighbors, indicating that a bright spatter has landed at that location on the powder bed. The LoG filter then homogenizes the image values globally, highlighting these local extrema. The reason why this cannot be detected directly on the original OT data image is that the local extrema can still have a relatively low value in a global context.

Figure 2.5 shows two areas on an OT image as represented in Figure 2.4. Each pixel in the images is marked with a value representing its global intensity. The area in Figure 2.5a has a lower value compared to figure 2.5b. However, the area on the left has a more rapid shift in intensity. The area highlighted in the right image has high values ranging throughout the area and also globally high values, as well as the change being more gradient. The areas both differ in intensity, although both contain locally extreme values.

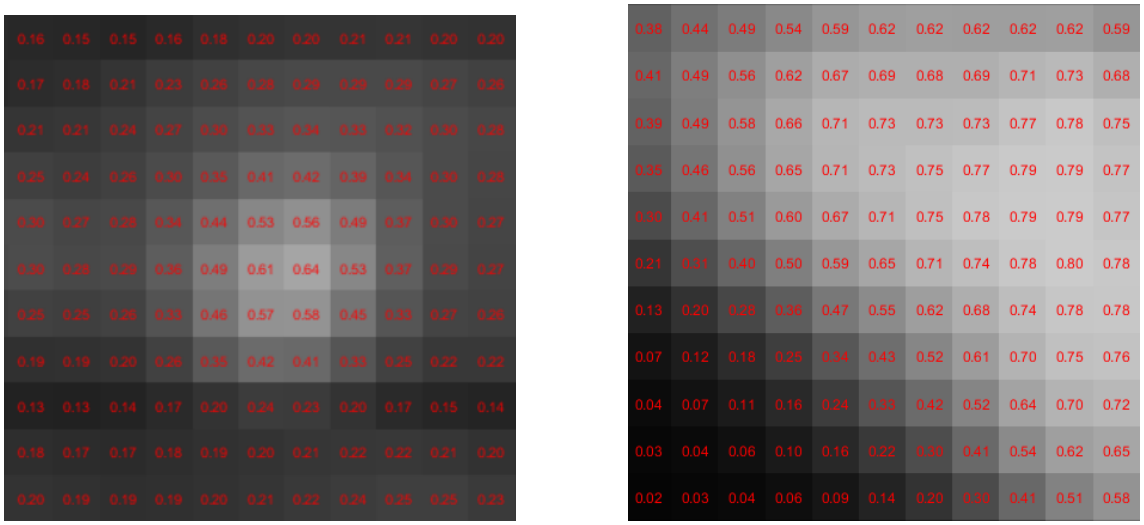

(a) Area with globally low intensity **(b)** Area with globally high intensity

Figure 2.5: Sections of OT image with varying intensity.

As seen in Figure 2.6 after the LoG filter has been applied, two local extrema that before filtration had a high intensity variation are still noticeable. However, now both have similar values and are now globally extreme, judging from the dark blue areas in the images global heat map.

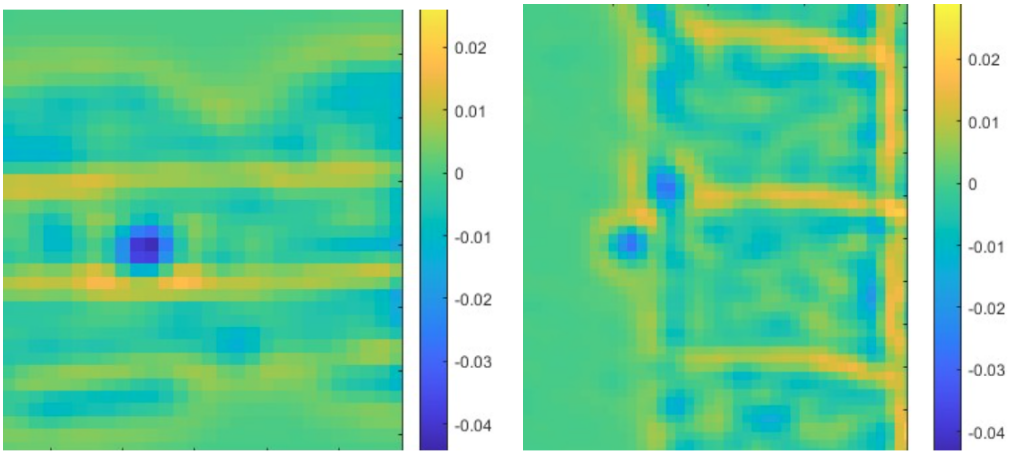

(a) Globally low intensity area after LoG filtration **(b)** Globally high intensity area after LoG filtration

Figure 2.6: Example images with homogenized intensity, where the heat map shows pizel values after filtration.

2.6 Inconel 718

Inconel 718 is a nickel-based superalloy that contains nickel, chromium and iron, with additions of niobium, titanium and aluminum [76] [77]. The mechanical properties of the alloy exhibit high strength, high creep resistance, excellent fatigue resistance

and good ductility [78] [79], while also maintaining these properties at temperatures up to 650°C. This makes it suitable for applications within the industrial sector, such as aircraft gas turbines, steam turbine power plants, nuclear reactors, and components for the aerospace industries. All of which where high strength and corrosion and oxidation resistance is critical [76] [80].

Due to its versatility and high performance, Inconel 718 is also commonly used in metal AM, specifically for Selective Laser Melting (SLM) and LPBF [78]. However, due to its hardness and low thermal conductivity, Inconel 718 presents challenges during the LPBF process. These challenges include porosity and poor surface finish [81], where the latter requires additional post-processing to achieve the desired surface.

2.7 Post-processing

Post-processing plays a critical role in additive manufacturing, especially when preparing parts for inspection, validation, or further use. In this study, several post-processing techniques were employed to segment the demonstrator components, preserve geometric integrity, and enable accurate dimensional analysis.

2.7.1 Abrasive water jet cutting (AWJ)

Abrasive water jet cutting (AWJ) is a nonconventional cutting process that is used in the automotive, aerospace, construction sector, etc. for its ability to cut through hard and soft materials [82]. It is often used to cut materials such as metals, super alloys, ceramics, composites, glass, rocks, or plastics. AWJ is a cold cutting process, which means that there are no heat-affected zones during the process and most often offers a clean and precise cut which does not require any additional machining to improve the surface finish.

The abrasive agents are used to change the cutting effect of the water jet. As different materials are cut, certain abrasives are more favorable to use to improve the cutting effect or reduce overall costs [83].

Table 2.1: Commonly used abrasives [83].

	Abrasive	**Cost**
1.	Sand	Low
2.	Garnet	Medium
3.	Aluminum oxide	Medium
4.	Emery	Expensive
5.	Iron residue	Low

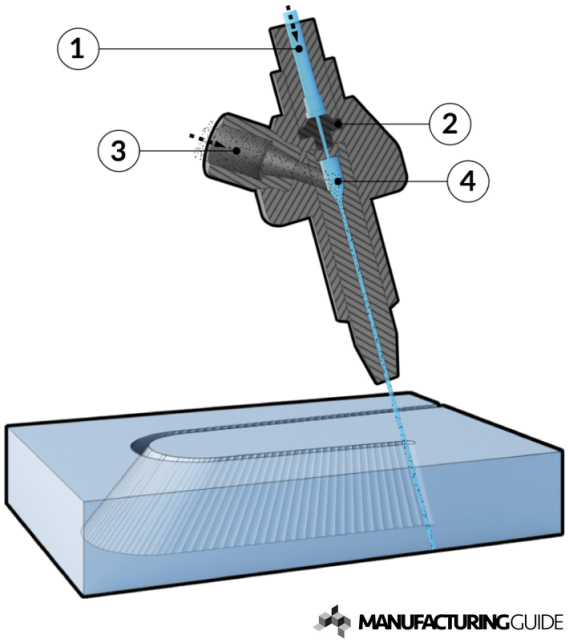

Figure 2.7: Illustration of the water jet process [84].

Table 2.2: Components of the water jet.

	Component
1.	High pressure water
2.	Orifice nozzle
3.	Abrasive agents
4.	Mixing chamber

The system operates by pumping water to high pressure, the orifice then transports the high-pressured water through the system to the high-velocity water jet. Before exiting the jet, the abrasive agents are mixed with the water in the mixing chamber, which is then charged out of the jet and cuts the material [85].

2.7.2 Wire cut Electrical discharge machining (EDM)

Wire Cut Electrical Discharge Machining (Wire EDM) is a machining process that uses electrical discharges (sparks) to erode material from a workpiece [86]. The process utilizes a wire for material removal by using a series of discrete electrical discharges between the workpiece and the wire [87]. The sparks can result in temperatures up to 10000 °C which melts and vaporize the material. The wire thickness often used varies between 0.1 and 0.4 mm in diameter depending on the material being processed [88].

The process is particularly effective for machining hard materials and for the manufacture of complex shapes with high precision [89]. The high temperatures require the workpiece to be submerged in a dielectric fluid that both cools the material and removes debris, see Figure 2.8 for a visual representation of the process.

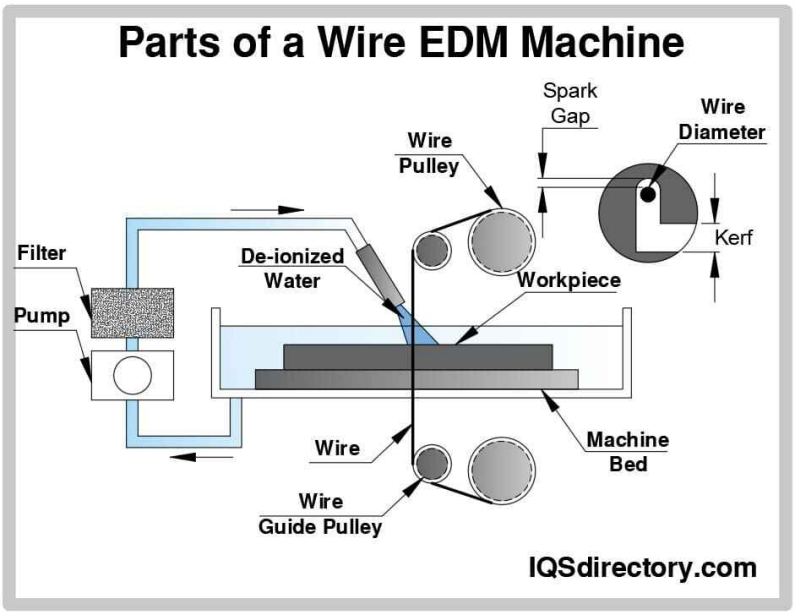

Figure 2.8: Illustration of the wire EDM process [90].

2.7.3 3D Scanning

3D scanning is a technology that captures the shape and dimensions of physical objects and converts them into digital 3D models. This process involves various techniques and tools, including high-resolution cameras, lasers, and advanced software, to create accurate and detailed representations of objects [91]. It is a widely used tool for manufacturers that requires accurate dimensional inspection, virtual image analysis, and prototype manufacturing. The virtual reconstruction can be used as validation for the manufacturing process by comparing the scanned sample to the original designs and tolerances. This can also be a good way to identify where in the manufacturing process any unwanted effect might occur by creating reverse models to identify them [92].

The 3D scanning of the demonstrators in this study was performed using the GOM ATOS ScanBox 6130, an automated optical 3D coordinate measuring system developed for high-precision digitization and inspection of large parts [93]. The ScanBox 6130 is well-suited for analyzing complex geometries and validating production parts against design specifications. The system supports components up to 3000 mm in diameter and weighing up to 2000 kg. With external dimensions of 4250 $\times$ 4250 $\times$ 2700 mm and a large opening width of 3100 mm [93]. The scanning process is fully automated, featuring a 7-axis kinematic system that enables comprehensive coverage of the component's surface. The ScanBox 6130 is compatible with high-resolution optical sensors, these sensors project structured light patterns onto the surface of the component and capture precise 3D data with high accuracy and repeatability [93].

Post-processing and inspection of the scanned data were performed using ZEISS INSPECT software. This software enables users to perform mesh editing, dimen-

sional analysis, and CAD comparison [94]. It features tools for evaluating geometric dimensions and tolerances, trend and deformation analysis, and digital assembly simulations. The software also supports 3D visualizations, inspection results, and statistical summaries [94].

3
Material & Methods

This chapter presents the materials and methods used during the project.

3.1 Inconel 718

In this study, Inconel 718 was used to manufacture the demonstrator for the engine mount due to the mechanical properties of the material, as mentioned in Section 2.6. The alloy was processed using LPBF. Some of the process parameters were intentionally chosen to induce the generation of defects, which is mentioned in more detail in Section 3.2. This was done to ensure the presence of detectable defects within the manufactured parts for analysis purposes.

3.2 LPBF process

To manufacture the demonstrator, an EOS M290 machine was used for its ability to produce high density and high precision components with complex geometries. This makes it especially suitable for demanding applications such as those found in the aerospace and energy sectors [95]. The system is equipped with a 400 W Yb fiber laser and offers a build volume of 250 × 250 × 325 mm, enabling the fabrication of both detailed features and relatively large parts [96]. In the context of this study, the consistency and high precision of the M290 ensured a controlled manufacturing environment where deviations could be introduced and analyzed.

The typical normal layer thickness for the machine is between 40-80 µm. However, to intentionally introduce more potential defects for analysis, the layer thickness for this build was set to 120 µm. Increasing the layer thickness reduces the number of layers needed, speeding up the build process. However, this also increase the chance that defects occur. A study by Pauzon et al. [97] demonstrated that increasing the layer thickness from 30 µm to 60 µm resulted in a 17% increase in the amount of spatter generated per scanned layer.

3.3 Process monitoring system

To evaluate the formation of defects during the LPBF process, this study relied on data collected by an in-situ process monitoring system. The primary source of monitoring was OT, a non-disruptive imaging method capable of capturing thermal radiation emitted during each layer's printing. This method offers insight into thermal effects such as spatter, lack of fusion, or abnormal heat distribution that could result in defects.

3.3.1 EOSTATE Exposure OT

The monitoring system used for this project was the EOSTATE Exposure OT system. This system facilitates non-destructive testing by automatically capturing optical tomography images of each layer during the additive manufacturing process. The EOSTATE Exposure OT system is equipped with a high resolution thermal imaging camera that continuously measures and records the exposure and melting of materials in real time [98]. As detailed in Section 2.3.1, the system was utilized to collect data on pixel intensity for every layer of the build.

The camera produces image outputs with a resolution of 2000 x 2000 pixels, where each pixel corresponds to 125 µm. For this project, the MAX images were used due to the simplified data processing of only using one channel of information (gray) while RGB contains three (Red, Green and Blue). The single channel of information potentially helps minimize noise in the image, making it more suitable for better contrast and edge detections. The images are subsequently saved in Tagged Image File Format (TIFF).

3.4 Data processing

In the initial phases of the project, the main focus was on processing the OT data collected during the LPBF process to find indications of spatter defects in the finished engine mount demonstrator. A MATLAB script was written as a way to automatically process OT images, the goal was to find local rapid changes in intensity and extrema in pixel values indicating abnormalities in the build that then could be filtered and sorted to finally compile points of interest with high defect indication density.

The images obtained from the OT system were stored as images with a 16-bit depth. Each pixel step represents 125 µm in a given direction. To make data handling more manageable when working with the code, these values were normalized to a range between 0 and 1. This normalization was performed to improve interpretability, as working with smaller values (e.g. 0.8) is more intuitive than handling the large values 16-bit would yield, such as 52,428.8/65,536 which is the 16-bit counterpart of 0.8. Figure 2.5 illustrates the grayscale values mapped on the original image, showing the transformation in the representation of values to values between 0 and

1. Spatter defects tend to manifest as smaller than 100 µm [99], which means that they would be small enough to only be shown in one pixel. However, since they also radiate light, they can give indications that manifest over a larger number of pixels in the final OT image.

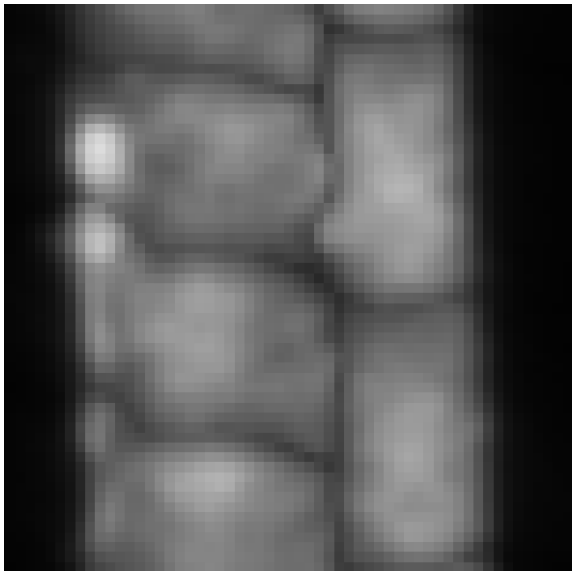

Figure 3.1: Section of OT image

3.4.1 Laplace of Gaussian and Erosion filtering

In the script, the LoG filter is implemented as a convolution matrix with predefined parameters. The first step involves specifying the size of the filter matrix, as this parameter directly influences the scale and sensitivity of edge detection. The matrix is then generated using a adjustable standard deviation, which controls the extent of Gaussian smoothing applied before the Laplacian operation.

Once created, the LoG filter is applied to the grayscale input image, shown in Figure **??**. The filter enhances edge-like structures by detecting regions of rapid intensity change. This process homogenizes the image, as demonstrated in Figure 2.6, where local extrema are transformed into global high values. The resulting image highlights potential defect regions, which indicate edges or transitions in intensity. The image after filtration can be seen in Figure 3.2.

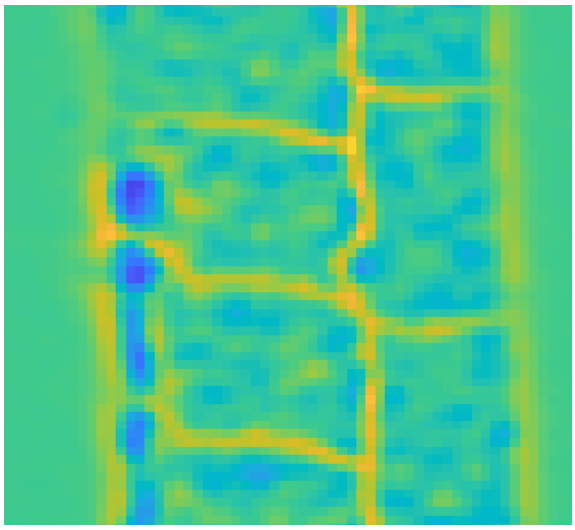

Figure 3.2: Section of OT image after LoG filtration.

After applying the LoG filter to the image, another filter is applied that erodes the image seen in figure 3.3, the erosion filter works by having a predefined matrix consisting of 1s, which determine how the filter relates to pixels neighboring the one focused on in each instance. The resulting image after the filter has been applied is less detailed and has larger chunks of homogenized pixels with sharper contrast to their environment rather than a more gradual change in their value. In addition to the sharper contrast, the filter also enhances extremes further as a result of the pixelation, making them stand out even more in relation to their environment and globally. This proved to be beneficial in the next thresholding step. The different parameters used for both filters play a great part in how different areas of the image are represented intensity-wise after they have been applied, as well as in how many pixels on the image are to be considered intense enough.

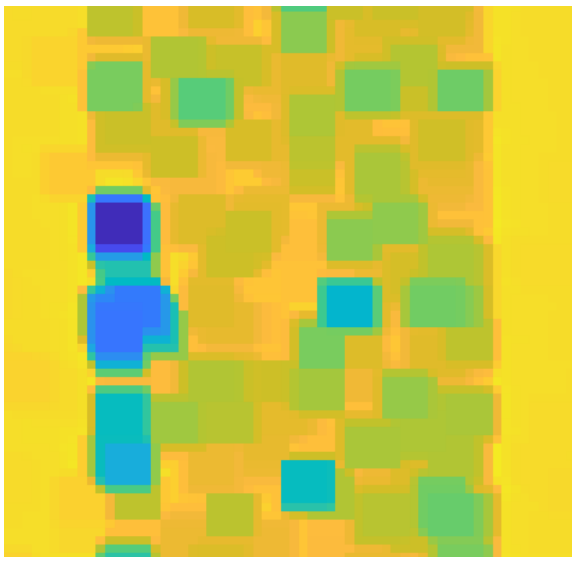

Figure 3.3: Section of OT image after erosion filtration

3.4.2 Thresholding

The next step in identifying deviations is setting thresholds that limit what the software in turn chooses to determine as deviations. After LoG and erosion filtration of the image, the first step in thresholding is an intensity measurement. The overall value range that pixels in the final filtered image can receive will vary based on what parameters have been used in the software, therefore, the intensity value for what can be considered an indication will vary. A threshold is set based on these parameters so that only pixels beyond a certain intensity are counted as an indication.

Pixels with an intensity that exceeds a preset intensity threshold are compiled in an array. The next step in the thresholding is locating all pixels exceeding the intensity that are also neighboring each other. Instead of counting each pixel that exceeds the threshold as a deviation they are all considered in a cluster. All these pixels in the cluster are then seen as a single deviation, a center point that represents the cluster is calculated based on the affected areas center point, which is rounded to be in the center of the nearest pixel. All center points are then compiled into another array that represents coordinates for the clusters center points.

This process was repeated for every layer of OT data collected throughout the manufacturing process. The collected deviations from all the layers are then compared across layers to determine if they are reoccurring. Reoccurrence across layers can be an indication that the area might be affected by an actual defect, as it both minimizes the risk of the software detecting false positives in the image and incorporates the possibility that the potential defect has healed in the fusion of the next layer. The software looks at the previously mentioned center points, and if there is one matching on the layer either above or below within a threshold of three pixels, they are recognized as neighbors. The indication must then be reoccurring for three consecutive layers in order to be considered, see Figure 3.4 for visual illustration. The last step of the image processing is to produce an array of reoccurring deviations that are then stored as a point cloud that, in turn, can be used for the digital comparisons.

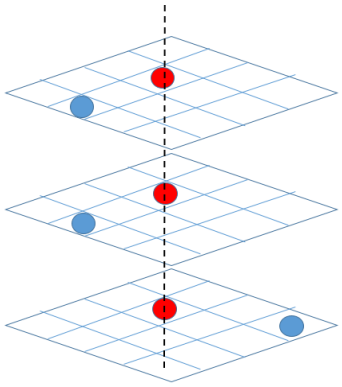

Figure 3.4: Illustration of three consecutive defect indications.

3.4.3 Digital comparison

A digital comparison of the indication points and a digital representation of the demonstrator was then made in order to see where the location of the points would correspond in the physical demonstrator. The point cloud produced by the image analysis code as well as a GOM scanned 3D representation of the physical demonstrator were compared. With the point cloud lined up, areas of interest with a high density of deviations could easily be seen and where they would correspond on the physical demonstrator, see Figure 4.1. With the digital comparison, a high indication density was found in the mounts of the demonstrator, as well as at the very top. With this information, a cut-up plan was made to perform the analysis.

3.5 Destructive part segmentation in preparation for X-Ray Computed Tomography inspection

The demonstrator needed to be cut into smaller pieces in order to lower the power we need to use to penetrate the sample, hence, it reduces the voxel size and gives higher resolution. These sections were based on the identified areas of interest of the demonstrator using the steps mentioned above in section 3.4. These areas were representations of where the most possible defects could be located given the density of the clusters generated from the point cloud.

As mentioned in Section 2.4.1, this study used the Phoenix V|tome|x M240 microfocus XCT system from Waygate Technologies to perform the XCT scans of the segmented parts. The machine uses a rotating platform that sits between the X-ray source and the detector. The machine then takes multiple 2D images from different angles to generate a 3D model from these images. Due to the dimensional limitations of the machine as well as beeing able to increse resolution, segmentation of the part was necessary. The machine can handle dimensions up to 420 mm Ø x 400 mm; however, due to the properties of Inconel 718, a diameter of 420 mm would not be possible for the machine to scan due to the high density of the material. To increase the precision of defect identification, segmented parts were chosen to be no thicker than 10 mm Ø.

Before segmentation and cutting, each section of the part that was intended to be cut was measured and marked to ensure traceability after the cutting. This was done by first marking each side of the mounts with a number (1-4) and then segmenting each side, numbering its position, for example, part 1 on side 3 received number 3.1 and part 2, 3.2 and so on. See Figures 3.5 and 3.7 for visual representation. In total, there were 36 segments planned to be cut, each a smaller section of larger areas, where all of these segments were from the mounts and top part of the demonstrator.

The cutting of the demonstrator was made in two steps, first an order was made to cut the part into smaller segments using an abrasive water jet. The image in Figure 3.5 shows the markings on the part where the segments were planned to be cut.

Figure 3.5: Isometric view before cutting.

After the first cutting process with the water jet, the part was cut in to 6 parts, both the mounts, the top part, the middle part and the bottom part of the demonstrator. See Figures 3.6, 3.7, and 3.8 that show the cut pieces in various orientations.

The second step in cutting the demonstrator was to cut the two mounts and top segment into smaller parts that in turn could be analyzed by the XCT scanner. After the first cutting process with the abrasive water jet it was clear that using the same procedure again was not feasible, as the smaller parts produced could risk falling out of the machine if not being properly fastened during cutting, which also could affect the quality of the cut. Instead, wire-cut EDM was used because of its ability to cut with gentler and smoother cuts, resulting in less material removal. By minimizing material removal, the alignment of the small parts with the digital point cloud would, in turn, be more accurate.

The two mounts and the top part were marked where the cuts were to be made, no larger than 10mm, and handed in for cutting. After the EDM process, the final result as previously mentioned, was 36 small segments numbered based on their location on the demonstrator, see Figure 3.9. The top of the demonstrator was segmented into 20 pieces, which varied in thickness since the top part had a slight elliptic shape and it was more efficient to not cut the parts at an angle. The mounts were first cut in half along their long side to reduce their thickness, originally they were 20mm thick which made them too large to yield valuable results in the XCT scan. Each half was cut into six parts, where the focus was to have four samples

Figure 3.6: Isometric view of mounts and top of part after first cut.

Figure 3.7: Side view of mount.

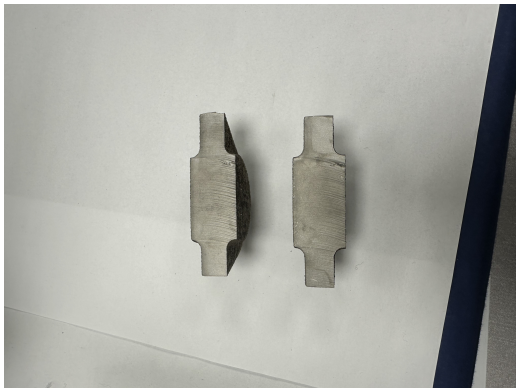

(a) Bottom view of cut mounts.

(b) Side view of both cut mounts.

Figure 3.8: Bottom view and side view of fasteners after cutting.

of the thicker middle, as they were considered both more interesting and feasible to examine due to their larger density of indications and shape.

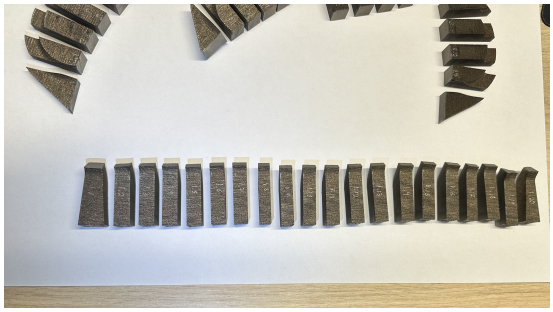

(a) Top part after cutting

(b) Mount 1

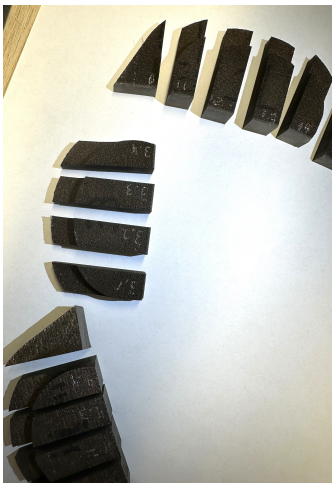

(c) Mount 2

Figure 3.9: Mounts and top part after additional EDM wire cutting.

3.6 XCT Parameter testing

After segmentation, all parts were scanned and analyzed using the XCT machine. To ensure optimal scan quality, different parameters had to be properly configured. This was achieved by conducting multiple test scans with different parameter settings to determine the most effective ones. All testing was carried out with a software expert, who provided guidance on which parameters to adjust and what aspects to prioritize. The parameters tested included the number of images, the number of averaged scans per angle, voltage, current, and voxel size (resolution). All scan parameters and their corresponding quality factors are presented in Table 3.1.

Table 3.1: Parameter testing

Test ID	Number of images	Timing (ms)	Averaging	Voltage (KV)	Current (μA)	Voxel size (μm)	Quality factor
1.1-1	900	150	3	200	170	30	7.07
1.1-2	900	250	8	200	170	30	6.23
1.1-3	900	250	8	170	130	20	7.07
1.1-4	900	250	12	190	180	30	7.44
1.1-5	900	250	12	220	160	30	7.41

The process began by first conducting a scan of sample 1.1-1 with generally applicable settings suited for similar samples, then analytically and visually interpreting the resulting reconstruction. The VGS software offers the ability to give an indicating value of the scans quality, also called the quality factor, the value is given by calculating the intensity contrast of the background in relation to the sample while also taking noise in between into account. Figure 3.10 shows two examples of scanned samples with their intensity compared to the background displayed in graphs, Figure 3.10a shows these peaks in the first scan with non optimized parameters, while Figure 3.10b has optimized parameters used in test 1.1-5, which were then used for the remaining samples. The main difference can be seen in the area between the two peaks, which gives an indication of how easy it is for the software to distinguish between background and sample.

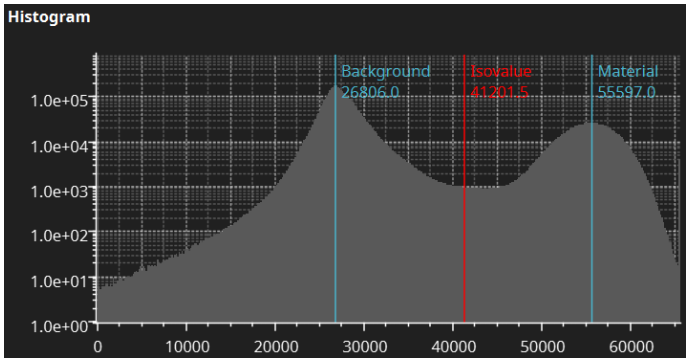

(a) Peaks from parameters used in scan 1

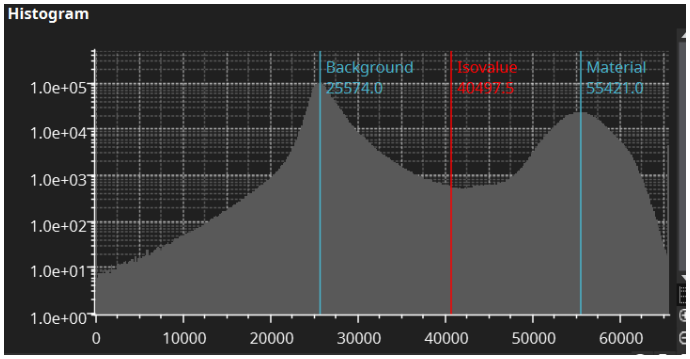

(b) Peaks from scans using final parameters

Figure 3.10: Graphs from first and final parameter tests.

The first test scan (1.1-1) was determined to have too much noise to be sufficient. The solution was to increase the number of average scans per angle, since then the XCT scanning software could compensate for the noise with the increased amount of scanning data. The reconstructed 3D model after the second scan (1.1-2) could then be analyzed again in the VGS software. After the parameter change, it was already considered to be more feasible and showed the internal structure in much better detail than what the first scan showed. Five test scans were conducted to determine which parameter set would yield the highest Q factor. Among the five configurations, the setup with an average increase of 12, a timing of 250 ms, 220 kV, and 160 µA at a resolution of 30 µm resulted in a Q factor of 7.41. Accordingly, sample 1.1-5 demonstrated the highest achievable image quality, and the study proceeded using this parameter set. All test scans were performed with an expert in the software and even if test 1.1-4 had a higher quality factor, the parameters from 1.1-5 would be more feasible for this thesis, due to the higher Kv of 220, which provided higher penetration and reproducible results. Except for the parameters presented in Table 3.1 all scans after 1.1-5 were scanned using two 0.5 mm tin filters that were placed in front of the X-ray source.

3.7 VGS Software Analysis

The scanned 3D rendering in VGS showed the external as well as internal structure of the scanned sample. The software offers the ability to visually phase through the sample to see cavities and how they occur throughout the sample. It also has the ability to automatically identify cavities throughout the whole sample and present them both visually and in a table, showing information such as probability of being a porosity, diameter, equivalent diameter, and coordinates of the cavities. This tool is especially useful, as it offers the ability to directly compare scan results with the previously produced point cloud. An edge-distance is needed as threshold for ensuring that the detection of porosities occurs inside the bulk material and do not include surface roughness falls indications.

Each scan with the chosen parameters took 60 min to complete and, given the time limit of the thesis, only a few of the samples was chosen to be analyzed. The samples chosen to focus on were both the mounts, as these showcased a higher density of indications based on the OT data as well as the absence of OT data for the very top layers of the demonstrator. In the end, it was determined that the samples decided to use in the analysis were the four middle pieces of each of the fasteners, seen in Figures 3.11.

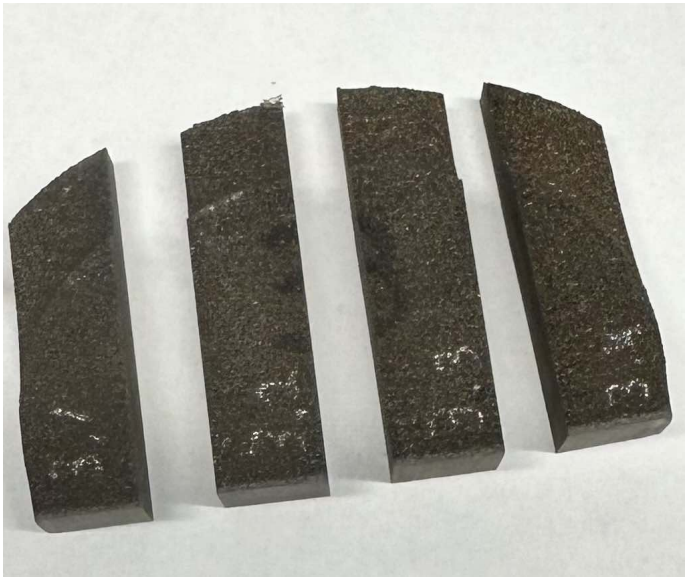

Figure 3.11: Center pieces for one side of one fastener

3.7.1 Alignment

After the samples had been scanned they were compiled in a single workspace in the VGS software. The alignment of the parts was made to reconstruct the demonstrator digitally in the VGS software. The alignment was performed by first creating planes tangent to the edges of the samples, more specifically the back, bottom and sides.

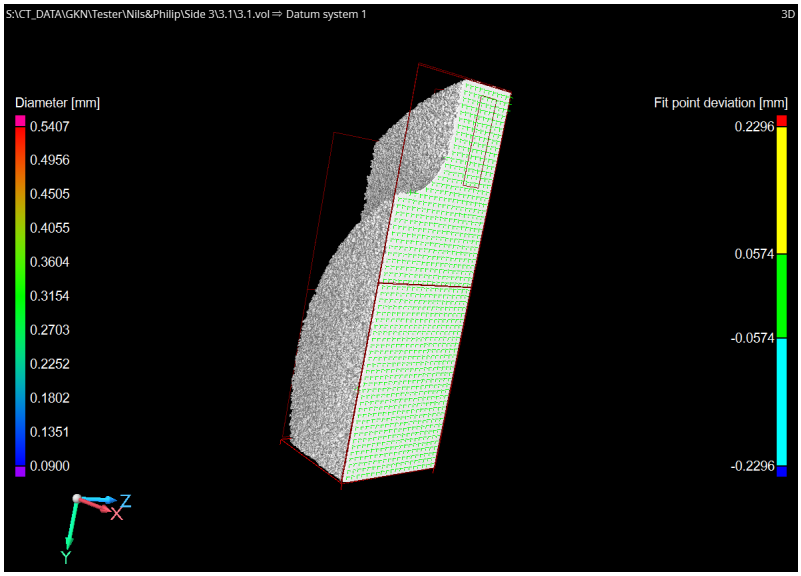

Figure 3.12: Side plane definition.

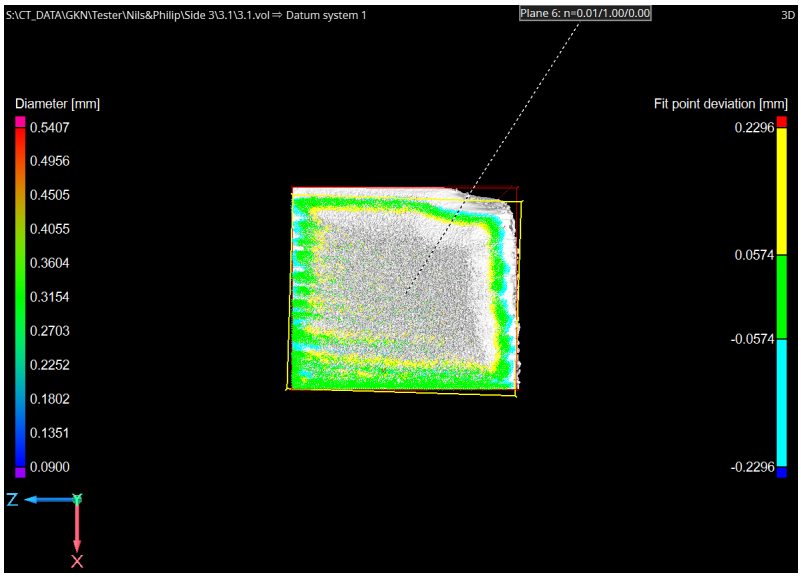

Figure 3.13: Bottom plane definition.

When creating the planes, the software generates a predetermined number of points along the sample surface and defines each plane as the average position of these points, as illustrated in Figure 3.12 and Figure 3.13. These planes were then used for alignment of the individual parts.

To compensate for material loss during the EDM cutting, an additional spacing of 0.32 mm was introduced between each sample when compiling them in the workspace. 0.32 mm was chosen because that was the size of the wire used to cut the parts. This was achieved by creating a new plane that was offset from the original using the transformation module in the VGS software, which moved the desired planes a distance that was manually chosen from the surface. Due to the inherent inaccuracy of the cutting process, the resulting surfaces varied in size and width, causing the samples' surfaces to not be completely parallel because of a difference in distance between the top and bottom. To mitigate this, manual measurement as well as manual rotation of the samples using the transformation module was necessary to achieve as close to parallel sides as possible. This alignment process had to be performed for each sample individually until the entire mount was properly recreated and aligned, as shown in Figure 3.15 and 3.14.

After reconstructing the mount, it needed to be aligned with the previously acquired GOM scan of the demonstrator. The GOM scan served as the reference for aligning both the mounts and the point cloud, as it was considered more representative of the actual manufactured part than the original CAD model. Alignment was achieved by defining corresponding geometric features, such as plane surfaces on the front and back, circular planes, and cylindrical surfaces, on both the mount and the GOM scan. The Sequential Alignment module was then used to match these features, enabling the alignment of planes, cylinders, and the top reference point. The result of this alignment is shown in Figure 3.16.

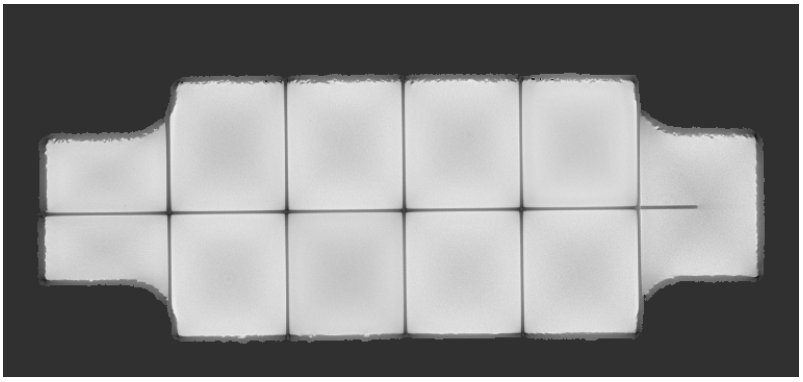

Figure 3.14: Alignment with additional spacing.

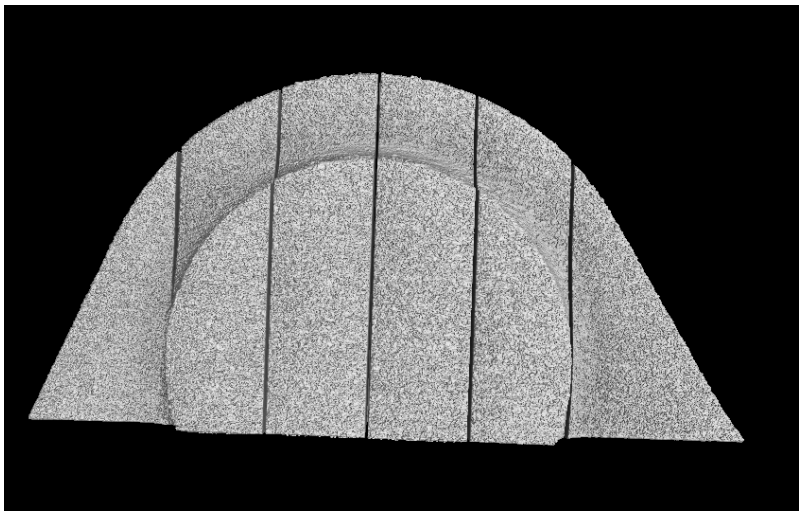

Figure 3.15: Mount after alignment.

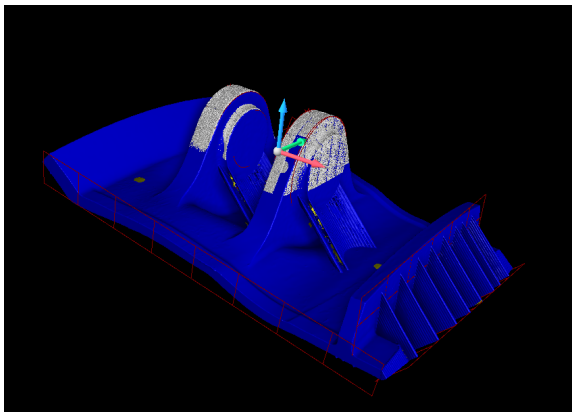

Figure 3.16: Mounts aligned with the GOM scan.

The next step involved aligning the point cloud generated by the MATLAB script described in Section 3.4. Since the VGS software can only align surface geometries, a mesh had to be generated from the OT point cloud. The software automatically created a surface mesh based on the point data, which was then aligned with the GOM scan using the Best Fit Alignment module. This module compares the two surface geometries and aligns them based on their most similar features. The result of this alignment is illustrated in Figure 3.17.

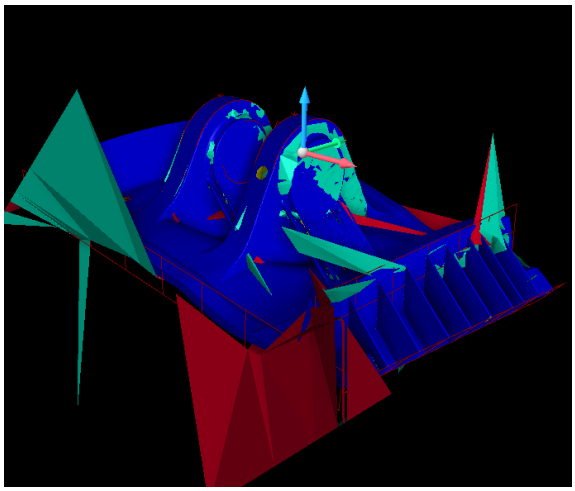

Figure 3.17: Surface mesh aligned with the GOM scan.

Since the surface mesh was generated from the point cloud, both the mesh and the point cloud share the same geometric features. As previously mentioned, the software does not support alignment of non-surface data. However, it is possible to transfer the transformation (coordinates and location) from an existing volume. This enabled the alignment of the point cloud with the surface mesh by simply copying and pasting the transformation. The results of this alignment are shown in Figures 3.18 and 3.19.

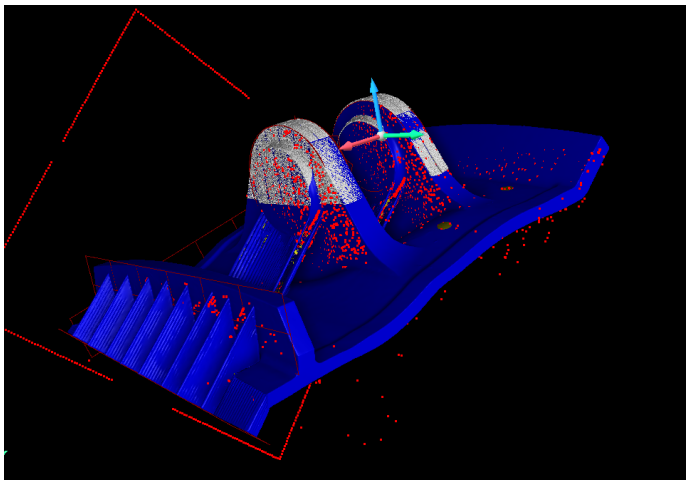

Figure 3.18: First Alignment.

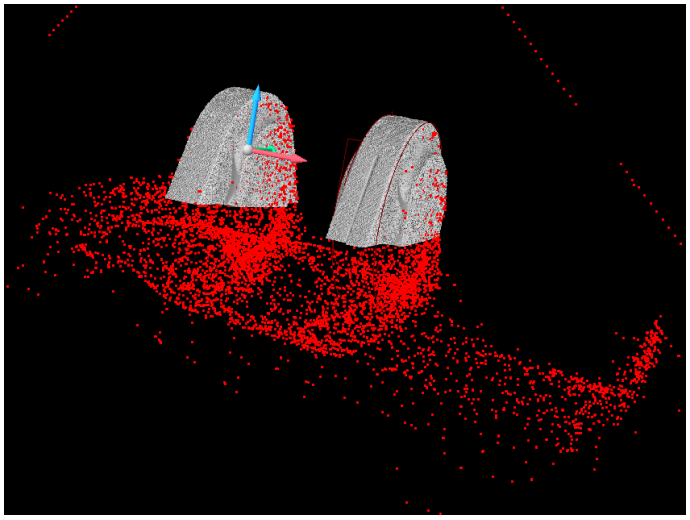

Figure 3.19: First alignment with mounts and big point cloud.

Following the initial analysis, a smaller point cloud was generated to focus specifically on the two mounts, as detailed in Section 3.9. This allowed for a more precise comparison between the identified areas from the script and the actual defects. The alignment process was then repeated for the smaller point cloud. First, a surface mesh was created from the new point cloud. This mesh was aligned with the GOM scan, and then the smaller point cloud was aligned with the surface mesh by copying and pasting the transformation from the mesh. The final alignment of the smaller point cloud with the mounts is shown in Figure 3.20, as well as the final alignment in Figure 3.21.

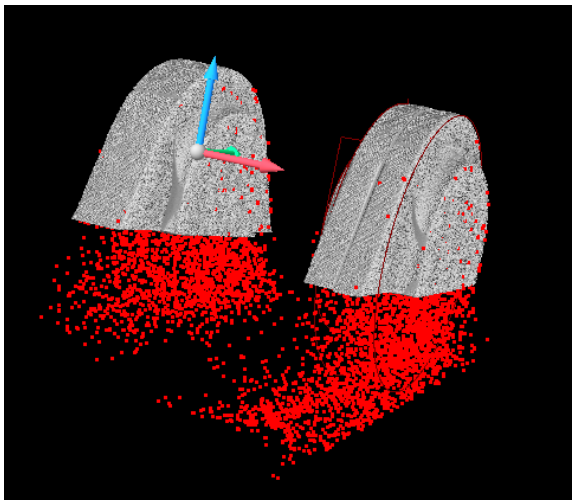

Figure 3.20: Alignment with reduced point cloud.

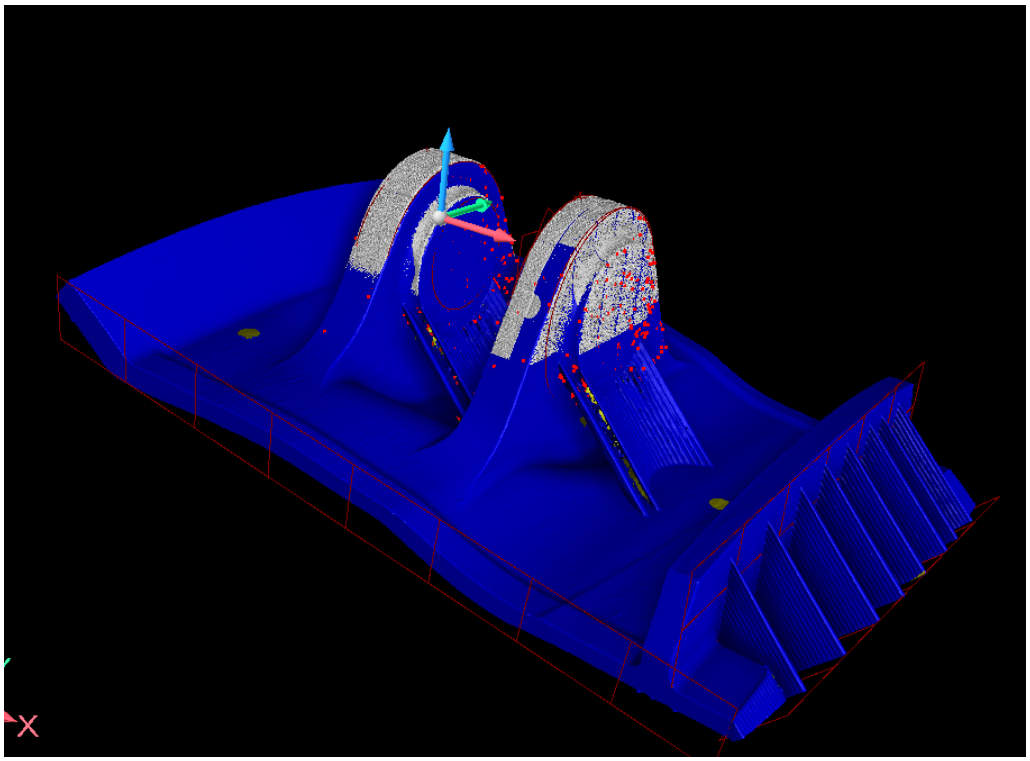

Figure 3.21: Final alignment.

3.7.2 Porosity analysis

The XCT data analysis was performed using built-in tools in the VGS software that allowed the analysis of both mounts separately. First, the outer surface was segmented using a gradient-based surface determination tool, it disregards a section of the most outer layer to not falsely detect surface roughness as pores in the material. The pores were then identified using the VGEasyPore module with sub-voxel accuracy, it automatically detects hollow and porous areas throughout the rendered

scanned sample based on various predetermined variables. A contrast value of 7% and a local area of 10 voxels were applied. Defects closer than 0.24 mm (8 voxels) to the surface were filtered due to the rough surface of the parts. In addition, a minimum probability threshold of 1 was implemented. The probability measurement in the software is used as a score for each detection, this score is represented in different values, and the higher the score, the higher the probability that an identified area is a defect. Finally, if the defect size was less than 0.09 mm in diameter (3 voxels), it was also excluded. The chosen parameters were based on a combination of manual testing and the guidance provided by experts familiar with the software. Their advice ensured that the parameters chosen were optimal for the specific context of this analysis. Figure 3.22 shows what it looks like in the software after a porosity has been found. It shows where in the object it is found from different angles so the operator can get a better overview.

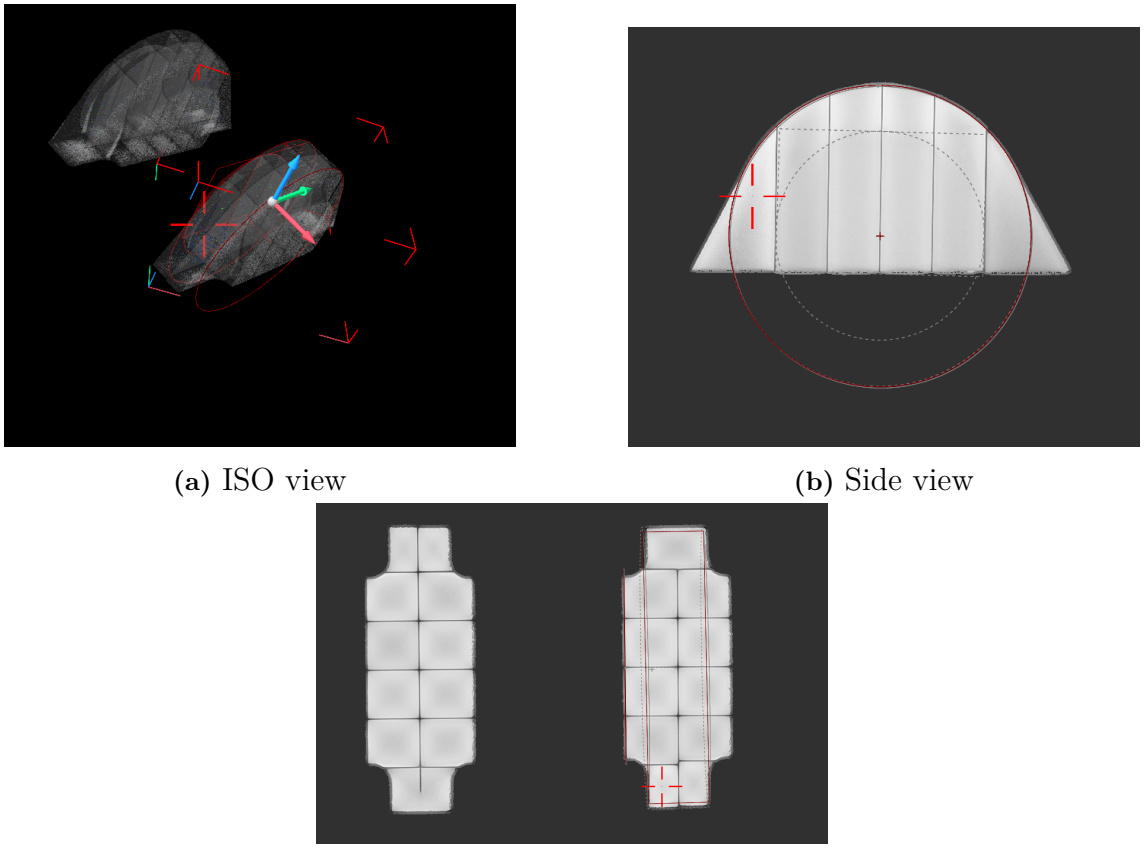

(a) ISO view

(b) Side view

(c) Top view

Figure 3.22: Different views of the porosity analysis

The software then generates an array of information about the identified pores and cavities in the material, the array consists of key information such as size of the defects and their location in the sample. This information was then exported into a CSV file for comparison with the original MATLAB script.

3.8 Script for data comparison

Data from the porosity analysis and point cloud was extracted from the VGS software after alignment in the form of CSV and text files. These files consisted of coordinates from both the point cloud and the structural analysis. As the point cloud had been moved within the workspace to align with the samples, its coordinates had also been changed to a new global coordinate system that was shared with the point cloud from the porosity analysis.

Then a script was written to compare the two arrays, find potential matches, and provide statistics. First, a threshold of 0.7 mm was implemented, this value was chosen because it takes the alignment issues and the fact that the OT analysis script and the VGS software identify the center point of indications differently, into consideration. The script then imports both arrays, compares each row of the first array to each row of the second one, and if the distance of the coordinates of a row are within the defined threshold, it is a match. Upon comparing all rows, the script provides a list of matching points, how many of them there are, their distance to the closest point. If multiple points match, the average distance between points within each list and how large of a percentage of points from each file are matching to the other.

3.9 Post-comparison

After the first comparison between the point cloud generated by the OT image processing script and the structural analysis, it was deemed that adjustments had to be made to the original code. This was because the result was not considered sufficient and multiple reasons for the poor correlation were identified. Firstly, a setting in the VGS software filtered out detections in its structural analysis that were near the edges of the samples. This was implemented to avoid having surface imperfections falsely considered as cavities and defects within the material, although it meant that all detections near edges by the code would not match in the comparison.

The solution was to implement an additional filter in the code that looked at the different detections location and how high its neighboring pixels intensity was on the original OT image. Then, if any neighboring pixel within a range of 3 pixels had an intensity lower than 0.09 (meaning it was close to black), it would not be considered, as this meant it was close to an edge.

In addition to this, a modification to the code was made so that it produces two separate point clouds. One of the point clouds had restrictions on what areas from the demonstrator to consider, while the other included all generated detections. This was made to have a point cloud that almost only included detections from the two mounts since detections from other areas of the demonstrator would guarantee mismatches in the comparison. The inclusion of the bigger point cloud was to still easily be able to align with the demonstrator in the VGS software and then match

the smaller point cloud to the rest of the components for the analysis.

The last modification to the script was to add the possibility of excluding certain coordinates of the two point clouds being compared to each other. For instance, a limitation could be added to not include any coordinates under a certain height. It was made to guarantee that they shared the same geometry before being compared to yield a more fair result.

3.9.1 Validation test

To evaluate the effectiveness of the image processing script developed for the demonstrator, a simpler part geometry, called a traveler, was also analyzed using the same defect detection approach. The travelers were printed simultaneously with the demonstrator using identical printing parameters and was printed as cylinders. Two different travelers were analyzed and served as a validation step to assess whether the method produced consistent results across different geometries. A total of eight travelers were printed with the demonstrator and can be seen in Figure 1.1.

To analyze the travelers, new XCT scans were performed using updated scanning parameters. These parameters were selected to enhance the resolution and detail of the scans, allowing for more accurate identification of pores within the part. The new scan settings are presented in Table 3.2 with the addition that traveler S-4 were scanned with a 0.6 mm Cu filter and travelers S-2 and S-4 limited with a 1 mm tin filter.

Table 3.2: Parameters for the travelers

Traveler	Number of images	Timing (ms)	Averaging	Voltage (KV)	Current (μA)	Voxel size (μm)
S-4	900	500	8	170	60	10.3
S-2 Limited	900	250	24	190	260	50
S-4 Limited	900	250	24	190	260	50

For Traveler S-4, the updated scanning parameters only allowed the top section of the cylinder to be scanned, primarily due to the great amount of time required for high-resolution scanning. In contrast, Travelers S-2 Limited and S-4 Limited (scanned with different settings) used parameters that enabled shorter scan times while still capturing the entire geometry of the cylinders and not just the top portion. These new parameters were chosen bqecause a voxel size of 50µm provided sufficient resolution (150µm) for detecting the minimum size defect.

The alignment process for the travelers followed the same procedure as the one used for the mounts, with an additional step required to achieve correct rotational alignment. Specifically, two manually generated reference lines were created to align with the engraved number "4" and "2" on the top surface of the cylinders. Figure 3.23 shows the example of the S-4 traveler. This was necessary due to the absence of

other distinctive reference features in the point cloud and enabled more accurate rotational positioning.

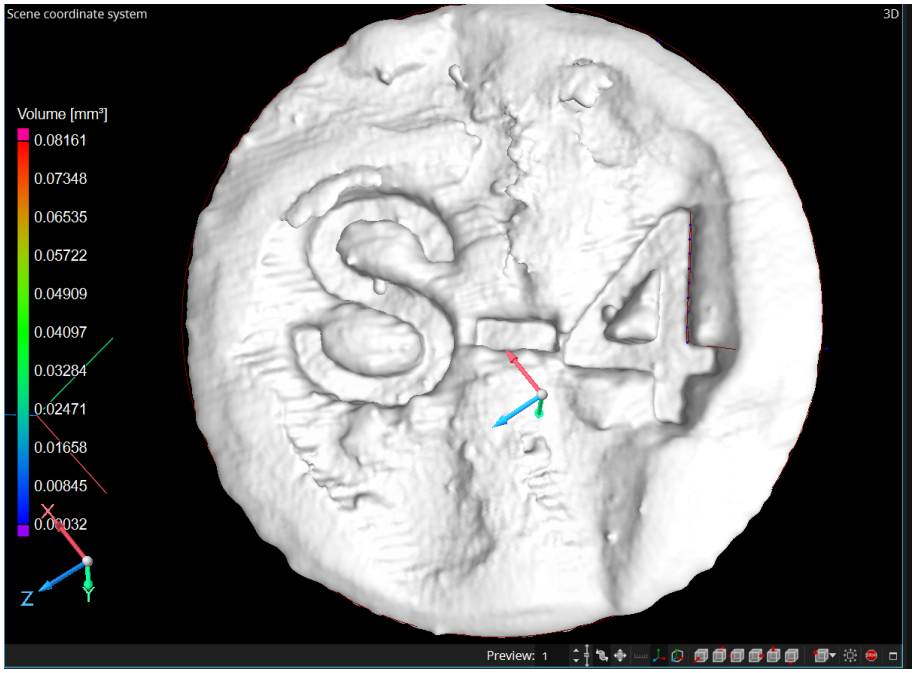

Figure 3.23: Example of the engraving used for rotational alignment of the travelers

To enable the image processing script to generate a point cloud for the travelers, the clustering step had to be removed, as it prevented any defect detections from being made. Additionally, a separate analysis was performed on the S-2 Limited and S-4 Limited travelers using an adjusted set of parameters for the analysis. In this case, a minimum pore size threshold of 180 μm was applied to focus on larger porosities.

3.9.2 Defect density

To further understand the distribution defects detected during the LPBF process, a defect density analysis was performed using tools in VGS. The goal of this step was to identify whether the investigated regions within the demonstrator differed in porosity concentration, which may suggest localized process instabilities or recurring sources of error during printing. For each segmented region, a defect density metric was extracted, expressed as the volume of indications per cubic millimeter.

4

Results

This chapter presents the results obtained from the image processing script, XCT analysis, digital comparisons and the validations performed on the demonstrator and traveler components.

4.1 Process Monitoring Data Analysis

The OT image processing script, detailed in Section 3.4, generated a point cloud consisting of 6085 indications throughout the demonstrator. These indications were identified based on rapid intensity changes in the gray value for each layer, which could suggest the presence of defects. The coordinates of each point were recorded and visualized in a 3D cluster as shown in Figure 4.1, which shows all the potential location of the defects.

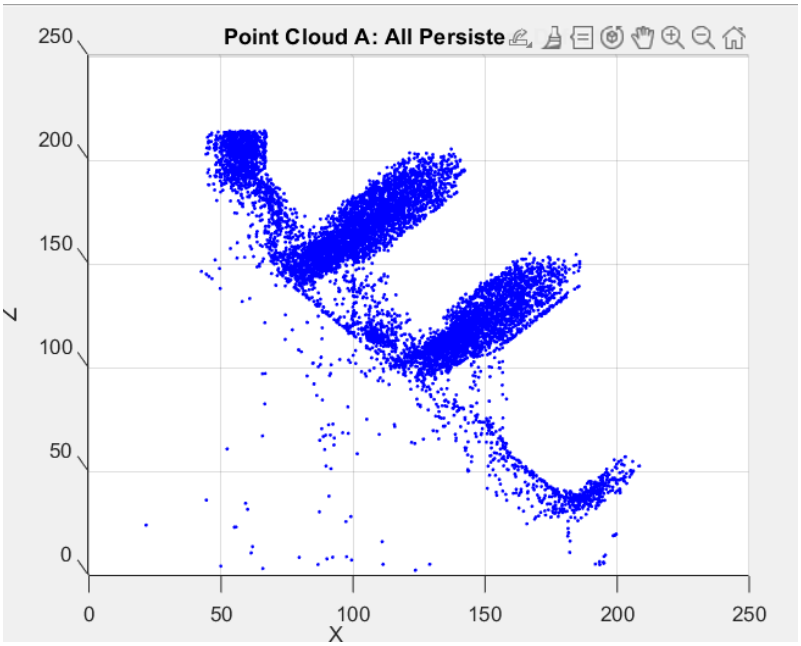

Figure 4.1: Point cloud of entire demonstrator generated from the MATLAB script

From this initial data, regions of interest were visually and quantitatively identified by locating areas with the highest concentration of points, as this could suggest

more actual defects being present. The Laplacian of Gaussian (LoG) and erosion filters were used to suppress minor noise and emphasized significant local maxima, which could indicate a defect being present.

From the resulting point cloud, areas of interest were visually identified by locating regions with the highest point density, as these were assumed to indicate a higher concentration of defects. These areas were then selected for further analysis.

4.1.1 Identified areas of interest

As shown in Figure 4.2, most of the filtered indications were concentrated around the two mounting structures and the top layers of the demonstrator.

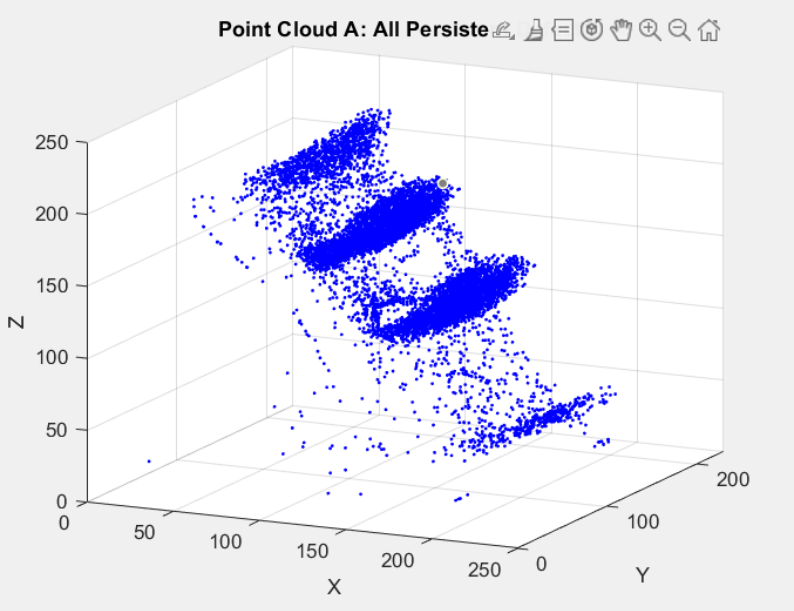

Figure 4.2: Point cloud from which areas of interest were identified

The mounts as well as the top part of the demonstrator were identified as primary areas of interest for further analysis due to their substantially higher density of anomalies. These findings were used as the basis for subsequent comparative evaluations using XCT scan data to investigate the presence of actual porosities, as mentioned in Section 3.8.

4.2 Porosity Analysis via XCT

The XCT scans were analyzed using the VGEasypore module in VGSTUDIO MAX to evaluate internal porosity. The porosity analysis module was applied to the entire reconstruction of the two mounts and was analyzed separately. The module then generated two separate lists of information for each one of them. These lists

included information such as the total number of porosities identified in the XCT scan, exact coordinates, size of the pores and sphericity. This information was subsequently visualized using the software, where both mounts were displayed in 3D. The generated porosity points were then overlapped within the mount geometries, allowing for clear visual representation of the internal defects, as shown in Figure 4.3.

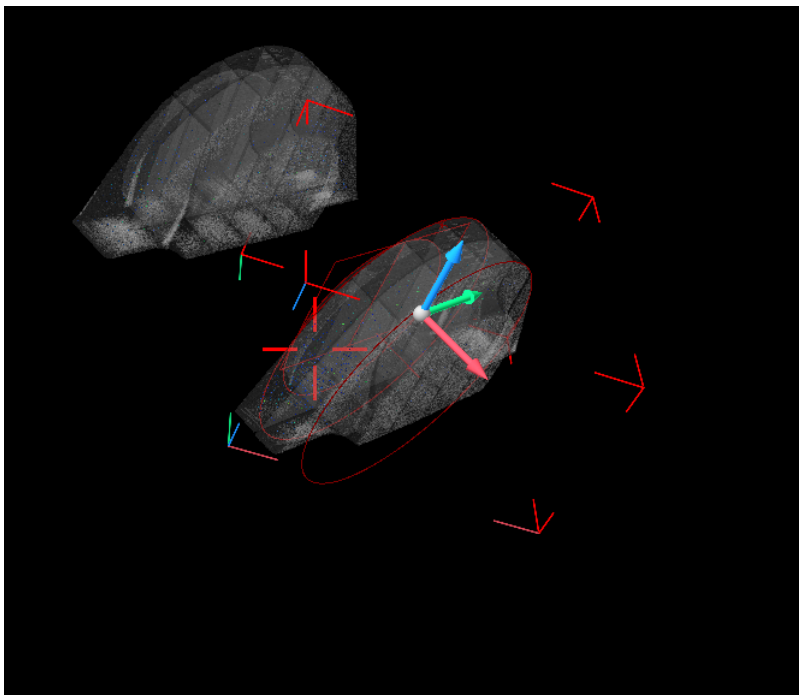

Figure 4.3: Porosity distribution identified through XCT analysis.

The porosity analysis of the different parts provided valuable insights as it was based on actual porosities detected within the components. From this analysis, information regarding the number of porosities, location and pore size of the defects could be extracted. Table 4.1 presents the total number of porosities identified in each part during the XCT scan, along with the corresponding minimum pore size thresholds applied in the analysis for each case.

Table 4.1: Porosity statistics for segmented parts.

Sample ID	Porosities identified	OT points	Min. pore size (μm)
Mount 1	3595	1231	90
Mount 2	3833	1649	90

4.3 Correlation Between In-Process Monitoring and XCT Results

As mentioned in section 3.9 additional geometrical filtration was made to the OT point cloud produced by the script, it was made to reduce the areas of indications to only include the mounts and disregard other parts of the demonstrator. The amount of indications in the point cloud was thus reduced to a total of 2562 points for both mounts. The physical defects identified through XCT scanning were subsequently compared with the indications from the OT based point cloud. This comparison was achieved by aligning both point clouds within the software environment and ensuring that they shared a common coordinate system, the two point clouds can be seen in Figures 4.4 and 4.5. The alignment procedure is described in more detail in Section 3.7.1.

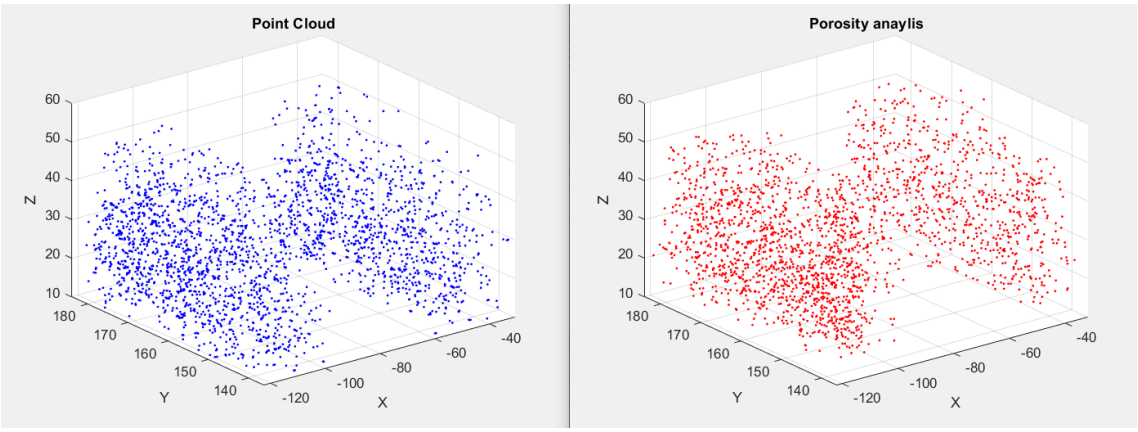

Figure 4.4: Isometric comparing view

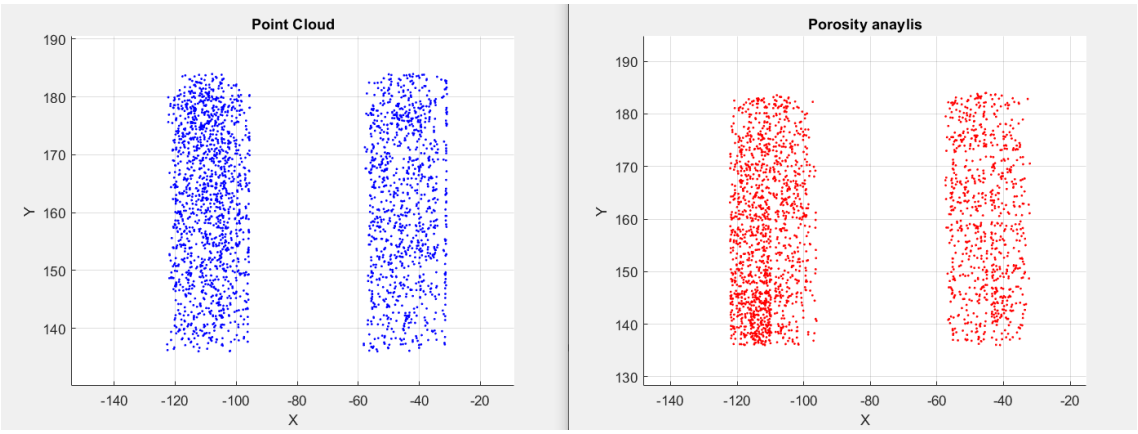

Figure 4.5: Top comparing view

From the correlation analysis, the result was a **~3%** correlation of the pores found via XCT with the identified points from the OT images as seen in Figure 4.6. This result was based on a 0.7 mm threshold, which means that every point that matches

between the two point clouds within 0.7 mm in any direction of another is a match. Further statistics on the sizes and heights of the defects can be seen in Figures 4.7a 4.7b

```
--- Porosity to Point Cloud Comparison ---
Total points in point cloud: 2880
Total porosity points (combined): 2204
Matches found (tolerance 0.70): 71
Percentage of porosity points matched: 3.22%
Percentage of point cloud points matched: 2.47%
```

Figure 4.6: Match statistics for demonstrator mounts.

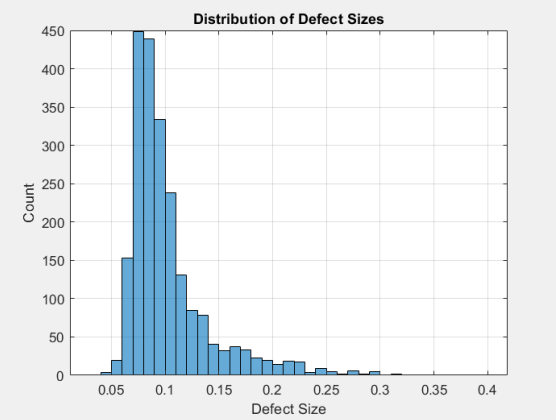

(a) Indication sizes for mounts

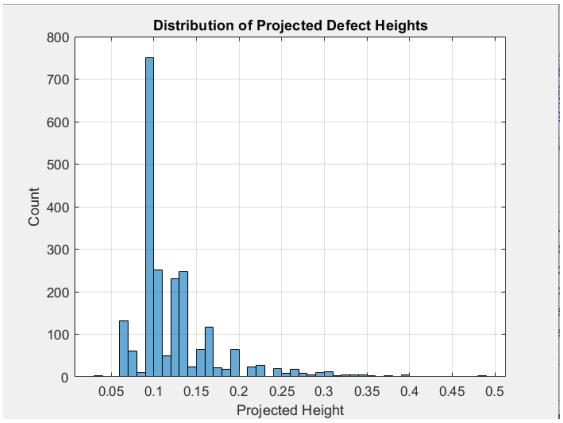

(b) Indication distribution for mounts

Figure 4.7: Graphs related to mount indications

4.4 Validation on simpler geometry

The same methodology was applied to the traveler samples, with the addition of a pore size threshold where only porosities with a minimum diameter of 180 μm were considered in the XCT-based analysis. These new pores were then compared with the defect indications identified from the OT images of each traveler, see Figure 4.8. The purpose of this comparison was to validate the detection method and to evaluate whether defects are more easily identifiable in simpler geometries. The resulting data for the travelers are presented in Table 4.2 and Figures 4.9, 4.10a and 4.10b.

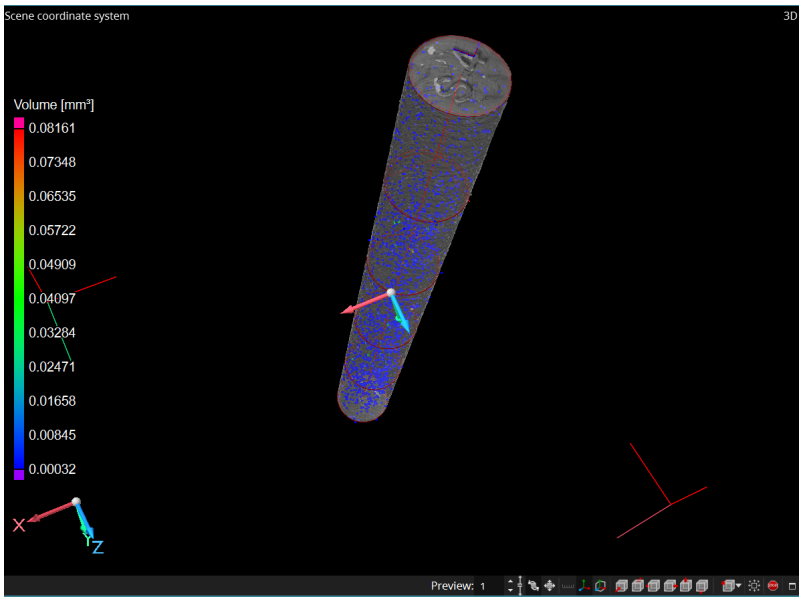

Figure 4.8: Final alignment of the traveler

Table 4.2: Porosity statistics for travelers

Sample ID	Porosities identified	OT points	Min. pore size (μm)
Cylinder S-4	5341	1787	90
Cylinder S-2 Limited	443	270	180
Cylinder S-4 Limited	395	1787	180

```
--- Porosity to Point Cloud Comparison ---
Total points in point cloud: 1709
Total porosity points (combined): 395
Matches found (tolerance 0.70): 155
Percentage of porosity points matched: 39.24%
Percentage of point cloud points matched: 9.07%
First 5 matches:
```

Figure 4.9: Correlation statistics for cylinder S-4 Limited.

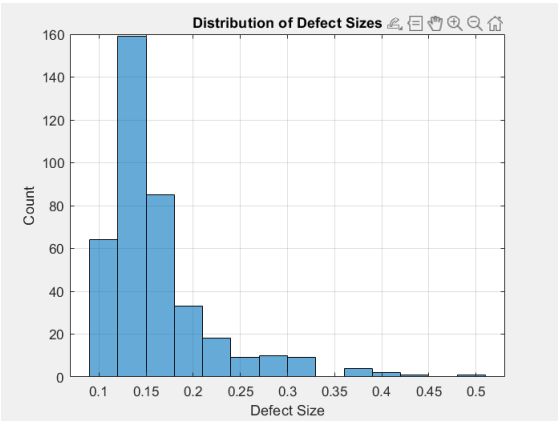

(a) Indication sizes for S-4 traveler

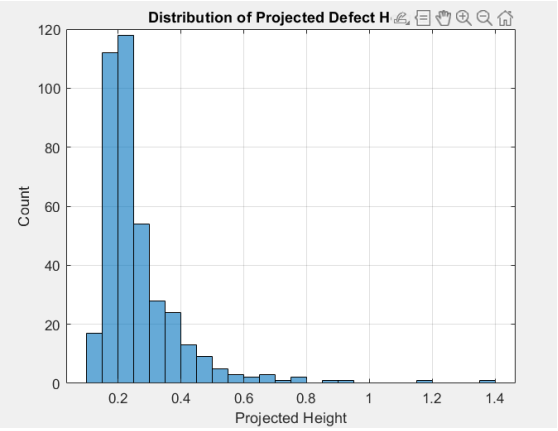

(b) Indication distribution for mounts

Figure 4.10: Graph of indication distribution for S-4 traveler

4.5 Summary of Findings

A summary of the correlation between the identified indications based on OT and the porosities detected by XCT scanning is presented in Table 4.3. The table also presents the percentage of matching porosities between the two point clouds, as well as the proportion of total matching points.

Table 4.3: Correlation of porosities and points

Part	Points OT	Points XCT	Matching Porosities	Matching points
Mounts	3160	2204	~3%	~2%
Mounts, no clustering	86793	2204	~70%	~2%
Cylinder S-4	1787	5341	~20%	~7%
Cylinder S-2 Limited	270	443	~2%	~3%
Cylinder S-4 Limited	1787	395	~39%	~9%

In addition to the porosity comparison, a defect density comparison was also performed and Figures 4.11 and 4.12 illustrates the result.

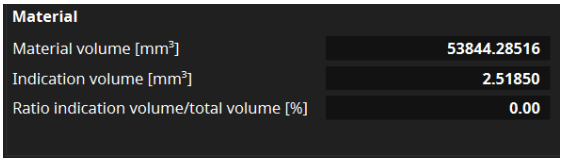

(a) Mount 1

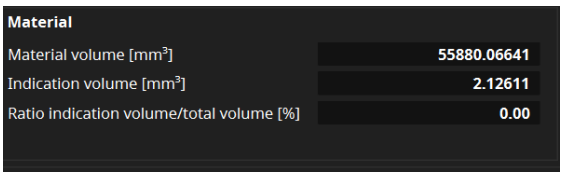

(b) Mount 2

Figure 4.11: Defect density of the mounts

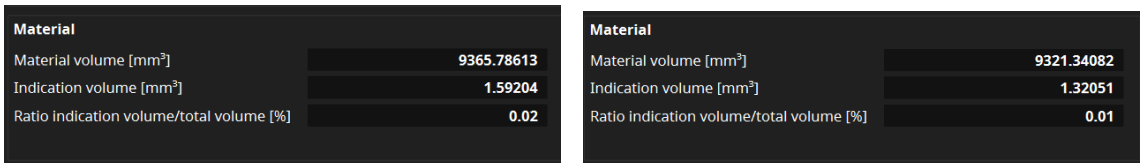

(a) Traveler S-2 **(b)** Traveler S-4

Figure 4.12: Defect density of the travelers

5
Discussion

This chapter discusses the significance of the results presented in Chapter 4, and the findings are interpreted in relation to the research questions, highlighting limitations. Furthermore, a comparison with an alternate method is made after a discussion with an expert in the field, looking at differences between the two methods and how they produce different results. Finally, opportunities for further work.

5.1 Evaluation of Process Monitoring Methods

The detection method showed approximately **3%** accuracy in identifying true internal defects (true positives) when comparing the porosity analysis to the point cloud and **2%** accuracy when comparing the point cloud to the porosity analysis instead. The reason for the difference in value was due to the different sizes of the two lists of coordinates. These results indicate that only a very small portion of actual defects observed by XCT were successfully predicted using the in-situ OT based image processing script. In addition, the low accuracy suggests that the code frequently flagged regions as defective when no corresponding defect was found in the XCT scan, resulting in a high rate of false positives.

This outcome highlights a significant limitation in the current detection approach. Although the methodology based on Laplace of Gaussian filtering and thresholding of OT images was effective at identifying high intensity thermal anomalies, it did not have the power to differentiate between process noise, false indications and defect-inducing spatter events. As a result, many of the identified areas did not translate into physical defects and many actual defects were completely missed.

Several factors may contribute to uncertainties throughout the process with the current method, the first one is the fact that there may be a mismatch in spatial resolution and depth. OT captures only surface-level thermal activity per layer, while many internal defects form due to subsurface dynamics, especially in thicker sections of the part. Secondly, the time-layer mismatch could be another cause. Pores may result from cumulative process variations or thermal build-up not isolated to a single OT frame, making detection difficult in a snapshot per layer. Another problem is the thresholding limitations. The various thresholds used throughout the filtration process may have been insufficiently optimized, leading to a large number of false detections. Noise amplification through the filtering process could also contribute, particularly erosion and LoG, may unintentionally highlight thermal gradients unre-

lated to physical flaws, such as edges or overhang transitions. Finally, OT pixel size. The size of the pixels on the OT images are 0.125 mm, meaning that any defect or deviation that does not present itself significantly on one or over several pixels will not be detected.

During a discussion with an expert in the field after the analysis had been performed, it was suggested that an entirely alternative methodology could potentially improve the correlation between OT-based indications and actual porosities. Specifically, adjustments to data alignment for validation, and filtering used in the image processing were highlighted as areas for improvement. For data alignment, it was suggested to not implement an automated approach to compare both data sets, as the current method does. Instead, manually compare the known clusters of indications with each other to validate the discovered indications. The suggested changes in the filtering method enabled this further. The changes discussed included the use of a different type of OT images, which would enable a method to identify the characteristics of the printed surface. Then, use this as the way to define defects, in addition to erosion filtering. This perspective supports the idea that the current approach is limited in its ability to capture true defects with high precision, even though it utilizes approved methods. Changing the method accordingly in future work could enhance the reliability of the process and lead to more accurate correlations.

As mentioned, the low correlation values underscore the need for improvements in the data analysis method. As the analysis of travelers showed, the large difference in the amount of detections did not correlate with the volume density of the defects in the parts analyzed. Moreover, the method could include more dynamic or adaptive thresholding throughout the OT analysis that looks at characteristics of indication like the expert had suggested, to reduce false detections.

5.2 Interpretation of Porosity Results

The porosity analysis through XCT scanning did reveal that pores existed in areas predicted by OT analysis to have a large amount of defects, although they did not share exact coordinates. Just as there were false positives, some porosity areas were found in regions where no previous anomalies had been detected, possibly due to limitations in the OT resolution or the timing of spatter formation and melt pool solidification, or due to uncertainties in exact coordinates because of the many uncertainties in the alignment process.

Just as there are false detections in the OT script, one type of defect that is detectable through XCT, yet does not produce clear indications in the OT data, is inhomogeneities within the powder bed. Since the mount corner parts, the mount samples furthest to the edges, were scanned using a different voxel resolution, the number of defects identified varied with other mount samples. This resulted in them having more small XCT detections than the remaining parts. Had they not been

removed from the comparison, it would have greatly affected the result, as a large number of small defects are not detectable in the OT analysis and could negatively impact the correlation result. Apart from the mentioned porosity related causes, a full list of limitations related to the whole project can be found below in Section 5.3.

Furthermore, the defect density analysis performed on both the demonstrator mounts and traveler cylinders in the VGS software showed that no significant variation in the amount of defect density was found between the different areas investigated. This is further confirmation that the used method is unreliable and using a fully automated OT analysis script to find defects is no certain way of finding defects, as the script had a large difference in the amount of defects found throughout the different samples.

5.3 Limitations of the Study

During the study several challenges were faced, limiting the results. These limitations arise from both the experimental setup and methodological choices made throughout the project. These limitations should be highlighted for the benefits of future work or refinement. The following sections describe the key limitations related to data acquisition, image processing, physical alignment, and overall project scope.

5.3.1 Image processing and detection challenges

The image processing script was designed to detect rapid changes in pixel intensity within the optical tomography images. While this method is effective in highlighting potential defect indications, it also introduces the risk of false positives, where non-defective features are mistakenly classified as defects. These inaccuracies may arise due to several factors, including the sensitivity of the applied thresholds or the presence of bright spots unrelated to spatter. Both the intensity and area thresholds play a critical role in detection accuracy. A low intensity threshold may result in a higher number of detections, but also increasing the likelihood of false positives being identified. While a threshold set too high may fail to capture actual defects, leading to false negatives. Similarly, the area threshold used during image processing also influences detection accuracy. A threshold set too narrowly may overlook defect indications that span slightly larger regions, leading to missed detections.

5.3.2 Alignment and segmentation limitations

The XCT scanner used in this study imposed limitations on the size of the parts it could analyze, necessitating destructive segmentation of the demonstrator. Although segmentation allowed for more accurate XCT scanning, particularly important for high-density materials such as Inconel 718, it also introduced several challenges in data reconstruction and alignment. Due to segmentation, parts had to be virtually reassembled within the analysis software to enable a complete evaluation.

This reconstruction step introduced multiple sources of potential errors.

Accurate alignment of the scanned parts was critical to ensure reliable results. Although the Volume Graphics software provides very good alignment tools, achieving high precision was challenging due to several factors. One key issue was the loss of material during the cutting process. As described in Section 3.7.1, an offset plane was introduced to compensate for the removed material. However, the cutting process did not produce perfectly parallel surfaces, leading to variations in the thickness of the removed sections. As a result, the applied offsets did not always accurately reflect the actual loss of material on the entire surface, requiring manual correction.

These manual corrections involved translational and rotational adjustments, which, despite best efforts, could not guarantee a perfectly accurate realignment. Moreover, after the physical segments were aligned, the OT point cloud generated from the image processing script also needed to be aligned to the reconstructed 3D model. Since the point cloud lacks a defined surface, the software performed the alignment automatically using geometric feature-based matching. Although these tools are effective, they rely on identifying similar features between the point cloud and the reference geometry, features that may not always match precisely. This introduces an additional source of potential misalignment and contributes to the overall uncertainty of the correlation between detected indications and XCT results.

Furthermore, aligning the cylinders with simpler geometries also required an additional method to ensure correct rotational positioning of the point cloud. As described in Section 3.9.1, this involved manually generating reference lines to match the text inscribed on the top surface of the cylinder, which helped to achieve the correct rotational alignment. However, similar to the approach used for the mounts, this method introduced uncertainties regarding the overall alignment accuracy and the final result.

5.3.3 XCT and Post-Processing Constraints

Although segmentation of the demonstrator improved the scan quality by allowing smaller parts to be imaged with higher resolution, it also made it impossible to assess the entire engine mounts in a single XCT scan. To maximize detail, the voxel size was reduced for the smaller segmented parts, which increased both the scan times and the volume of data generated. Due to the extended scan durations and the overall time constraints of the project, it was decided that only the mounts would be scanned and analyzed, while the top section of the part was excluded. This reduction in the total scanned area may have influenced the completeness of the results. However, based on the high density of defect indications identified in the mounts through the MATLAB script, it was considered that focusing on these areas would be sufficient to meet the objectives of the study.

5.3.4 Scope limitations

As mentioned in Section 1.4, there were certain scope limitations for this project. These limitations included only focus on stochastic spatter generated defects, only using Inconel 718 as material and use the EOS M290 for in-process monitoring.

All in-situ monitoring data were obtained using an EOS M290 LPBF system. Since all OT data were precollected, these parameters could not be affected during the project and only the MAX imaging could be used.

5.4 Future Work

One potential direction for future work is to improve the image processing script by incorporating a machine learning algorithm, such as a Convolutional Neural Network (CNN). The current approach is based on a more traditional image processing technique such as the Laplacian of Gaussian filtering, which risk producing false positives and may struggle with varying defect shapes, sizes, or noise levels.

Moreover, while machine learning could be a useful next step for improving defect detection in OT data. It might work especially well for certain types of defects such as keyholes or lack of fusion, where patterns are easier to spot. However, these methods need a lot of high-quality labeled data to learn from, which can be time-consuming to gather.

Another important step would be to further validate the use of OT images for defect detection by testing the approach on different materials and LPBF systems. This would help determine whether the method can be used generally and is reliable across various setups, rather than being limited to specific conditions.

Another direction for future work could be to incorporate Melt Pool Monitoring (MPM) data into the defect detection process. Unlike OT, which captures images layer wise, MPM provides real time insights into the thermal behavior of the melt pool during the build process. By analyzing the melt pool dynamics, it could be possible to directly correlate process irregularities with the formation of defects such as keyhole pores or lack of fusion [100].

MPM could contribute to a deeper understanding of the process by allowing analysis of melt pool dynamics and enabling correlations between thermal signatures and process parameters such as scan speed and laser power. This insight could support more effective parameter optimization strategies and help develop robust defect detection systems that generalize across materials and LPBF machines.

Currently, the alignment is highly sensitive to errors due to noise, distortions, or lack of reference points in the OT data, making it difficult to achieve a precise match in the software. As the match is not precise, the current method also relies on manual alignment of the parts. This misalignment can significantly affect the accuracy of

the defect location and the overall analysis.

To address this, future work could focus on developing or integrating a tool that saves reference points directly from OT data during the build process. By using these reference points, such as known surfaces or edges, it would be easier to align the OT point cloud with the corresponding CAD model or 3D mesh. This improved alignment capability could help bridge the current gap in the lack of reliable data points and lead to more reliable and accurate defect detection results and could be the reason why such a low correlation was achieved in this study.

6
Conclusion

This thesis has evaluated the possibility of using OT image data for the detection of internal porosities due to spatter in parts manufactured using LPBF. Additionally, some validation steps were used to ensure the reliability of the result and the method itself.

6.1 Correlation of OT images and defect detection

The aim of this thesis was to evaluate whether in-situ monitoring data, specifically from Optical Tomography (OT), could be used to predict and localize defects in metal parts produced using the Laser Powder Bed Fusion (LPBF) process. The demonstrator component, manufactured using Inconel 718, was analyzed through a combination of image processing, XCT scans, and data comparisons.

From the results in Chapter 4 it is clear that OT images can not be used to accurately detect defects during the LPBF process. The results suggest that only 3% of the points of interest found in OT was actual defects based on the porosity analysis from the XCT scan. However, it was also clear that it was possible to achieve a higher correlation of matching porosities if the clustering between multiple layers was removed. This, on the other hand, allowed the possibility of including more false positives as the matching points only were 2%.

Furthermore, the validation steps provided a slightly better result with a porosity value matching of 2-39% depending on the traveler analyzed and the chosen parameters. In the best case Cylinder S-4 with a limitation parameter of only allowing pores with a minimum diameter of 180 μm achieved a correlation of 39% when comparing porosities to the point cloud, however, it still had a correlation value of only 9% when comparing the point cloud to the porosities. Since the same method was applied across all traveler segments, the higher correlation in Cylinder S-4 may suggest that parts with more complex geometries produce defects that are more difficult to detect using the OT method, either due to limitations in the image processing approach or challenges in achieving accurate alignment.

However, as mentioned in Section 5.1, similar studies done on the topic have shown higher correlations using different methods. Which could suggest that the image processing script is not effective enough. By optimizing the first step of the process,

the possibility of achieving a higher correlation could be possible.

The study shows that with the method used and the constraints and limitations mentioned, OT images can not be used to accurately identify defects generated by spatter (**RQ1**).

OT image processing and analysis using the method presented in this project has several limitations in detecting internal porosities in LPBF. A major challenge is the low correlation when directly comparing the OT indication point cloud to the XCT defect coordinates, mainly due to the large number of false positive OT detections, stemming from the way the script notices indications and the difficulties in tuning all parameters and thresholds. In addition to this, OT has a lower resolution than XCT and an inability to capture defects caused without a change in heat signature. On top of this, there are big challenges in the alignment process once the two analyses have been completed. To address these issues, the study suggests using another type of OT images, or a combination of variants of OT data, that capture not only the maximal heat signature of a pixel. In addition, using more adaptive thresholding when analyzing the OT data and implementing machine learning as a way to classify defects directly from the OT. Finally, implement a method to create reference points directly in the OT data for a more accurate process to align OT indications to known defects **(RQ2)**.

6.2 Final Remarks

To summarize, this thesis shows that the current method used for predicting defects using OT images is not sufficient to achieve a high level of correlation with actual porosities. The combination of constraints and limitations, and a basic image processing script contributed to a low accuracy in identifying true positives. However, with improvements to the image processing algorithm and by incorporating the recommendations outlined in Section 5.4, the potential for this approach to become more reliable and accurate could be significantly enhanced.

References

[1] S. Feng, Z. Chen, B. Bircher, Z. Ji, L. Nyborg, and S. Bigot, "Predicting laser powder bed fusion defects through in-process monitoring data and machine learning," *Materials & Design*, vol. 222, p. 111 115, 2022, ISSN: 0264-1275. DOI: https://doi.org/10.1016/j.matdes.2022.111115. [Online]. Available: https://www.sciencedirect.com/science/article/pii/S0264127522007377.

[2] V. Thakur, R. Singh, and R. Kumar, "Chapter two - materials for additive manufacturing in clinical podiatry," in *3D Printing in Podiatric Medicine*, K. Sandhu, S. Singh, C. Prakash, K. Subburaj, and S. Ramakrishna, Eds., Academic Press, 2023, pp. 35–50, ISBN: 978-0-323-91911-1. DOI: https://doi.org/10.1016/B978-0-323-91911-1.00006-7. [Online]. Available: https://www.sciencedirect.com/science/article/pii/B9780323919111000067.

[3] S. R. Narasimharaju, W. Zeng, T. L. See, *et al.*, "A comprehensive review on laser powder bed fusion of steels: Processing, microstructure, defects and control methods, mechanical properties, current challenges and future trends," *Journal of Manufacturing Processes*, vol. 75, pp. 375–414, 2022, ISSN: 1526-6125. DOI: https://doi.org/10.1016/j.jmapro.2021.12.033. [Online]. Available: https://www.sciencedirect.com/science/article/pii/S1526612521009178.

[4] G. Aerospace. "Gkn aerospace - advancing aerospace technology." Accessed: 2025-02-03. (2025), [Online]. Available: https://www.gknaerospace.com/.

[5] A. Kumar, S. C. Kaushik, and S. N. Garg, "A review of multi-criteria decision making (mcdm) towards sustainable renewable energy development," *Renewable and Sustainable Energy Reviews*, vol. 69, pp. 596–609, 2019, ISSN: 0278-6125. DOI: 10.1016/j.rser.2016.11.191. [Online]. Available: https://www.sciencedirect.com/science/article/pii/S0278612519300731.

[6] T. Sonar, V. Balasubramanian, S. Malarvizhi, T. Venkateswaran, and D. Sivakumar, "An overview on welding of inconel 718 alloy - effect of welding processes on microstructural evolution and mechanical properties of joints," *Materials Characterization*, vol. 174, p. 110 997, 2021, ISSN: 1044-5803. DOI: https://doi.org/10.1016/j.matchar.2021.110997. [Online]. Available: https://www.sciencedirect.com/science/article/pii/S1044580321001273.

[7] S. Chowdhury, N. Yadaiah, C. Prakash, *et al.*, "Laser powder bed fusion: A state-of-the-art review of the technology, materials, properties & defects, and numerical modelling," *Journal of Materials Research and Technology*, vol. 20, pp. 2109–2172, 2022, ISSN: 2238-7854. DOI: https://doi.org/10.1016/j.jmrt.2022.07.121. [Online]. Available: https://www.sciencedirect.com/science/article/pii/S2238785422011607.

[8] Z. Hasan, "Chapter 8 - future lookout," in *Tooling for Composite Aerospace Structures*, Z. Hasan, Ed., Butterworth-Heinemann, 2020, pp. 231–240, ISBN: 978-0-12-819957-2. DOI: https://doi.org/10.1016/B978-0-12-819957-2.00008-0. [Online]. Available: https://www.sciencedirect.com/science/article/pii/B9780128199572000080.

[9] U. M. Dilberoglu, B. Gharehpapagh, U. Yaman, and M. Dolen, "The role of additive manufacturing in the era of industry 4.0," *Procedia Manufacturing*, vol. 11, pp. 545–554, 2017, 27th International Conference on Flexible Automation and Intelligent Manufacturing, FAIM2017, 27-30 June 2017, Modena, Italy, ISSN: 2351-9789. DOI: https://doi.org/10.1016/j.promfg.2017.07.148. [Online]. Available: https://www.sciencedirect.com/science/article/pii/S2351978917303529.

[10] S. Rudge, "The future of additive manufacturing: Top 7 applications," *Manufacturing Today*, Sep. 2024. [Online]. Available: https://manufacturing-today.com/news/7-key-uses-of-additive-manufacturing-driving-innovation-in-the-next-decade/.

[11] I. Gibson, D. W. Rosen, B. Stucker, *et al.*, *Additive manufacturing technologies*. Springer, 2021, vol. 17.

[12] F. Bosio, A. Aversa, M. Lorusso, *et al.*, "A time-saving and cost-effective method to process alloys by laser powder bed fusion," *Materials & Design*, vol. 181, p. 107 949, 2019, ISSN: 0264-1275. DOI: https://doi.org/10.1016/j.matdes.2019.107949. [Online]. Available: https://www.sciencedirect.com/science/article/pii/S0264127519303879.

[13] P. Cobbinah, R. Nzeukou, O. Onawale, and W. Matizamhuka, "Laser powder bed fusion of potential superalloys: A review," *Metals*, vol. 11, p. 58, Dec. 2020. DOI: 10.3390/met11010058.

[14] W. Abd-Elaziem, S. Elkatatny, A.-E. Abd-Elaziem, *et al.*, "On the current research progress of metallic materials fabricated by laser powder bed fusion process: A review," *Journal of Materials Research and Technology*, vol. 20, pp. 681–707, 2022, ISSN: 2238-7854. DOI: https://doi.org/10.1016/j.jmrt.2022.07.085. [Online]. Available: https://www.sciencedirect.com/science/article/pii/S2238785422011243.

[15] E. Malekipour and H. El-Mounayri, "Common defects and contributing parameters in powder bed fusion am process and their classification for online monitoring and control: A review," *The International Journal of Advanced Manufacturing Technology*, vol. 95, Mar. 2018. DOI: 10.1007/s00170-017-1172-6.

[16] M. Grasso and B. M. Colosimo, "Process defects and in situ monitoring methods in metal powder bed fusion: A review," *Measurement Science and Technology*, vol. 28, no. 4, p. 044 005, 2017.

[17] B. TRANCHAND, J. Hugues, and S. Perusin, *Common defects in powder bed fusion technologies*, Nov. 2019.

[18] L. Cordova, A. M. Khorasani, T. Bor, I. Gibson, M. Campos, and T. Tinga, "Melt pool monitoring for the laser powder bed fusion process," English, in *Euro PM 2019 Congress and Exhibition: European Powder Metallurgy Congress and Exhibition, Euro PM 2019*, Maastricht, Netherlands: European Powder Metallurgy Association (EPMA), Oct. 2019, ISBN: 978-189907251-4.

[19] M. Baier, M. Sinico, A. Witvrouw, W. Dewulf, and S. Carmignato, "A novel tomographic characterisation approach for sag and dross defects in metal additively manufactured channels," *Additive Manufacturing*, vol. 39, 2021. DOI: 10.1016/j.addma.2021.101892. [Online]. Available: https://www.scopus.com/inward/record.uri?eid=2-s2.0-85100661308&doi=10.1016%2fj.addma.2021.101892&partnerID=40&md5=96115a698377568649cf46bca8566ef3.

[20] F. Zanini, N. Bonato, and S. Carmignato, "Evaluation of defects in laser powder bed fusion metal parts via in-process optical measurements and post-process x-ray computed tomography," 2021, pp. 301–302. [Online]. Available: https://www.scopus.com/inward/record.uri?eid=2-s2.0-85109212488&partnerID=40&md5=842dcf0f6faebbe42abf4126c9bcf46d.

[21] S. Brenner, M. Moser, L. Strauß, V. Nedeljkovic-Groha, and G. Löwisch, "Recoater crashes during powder bed fusion of metal with laser beam: Simulative prediction of interference and experimental evaluation of resulting part quality," *Progress in Additive Manufacturing*, vol. 8, no. 4, pp. 759–768, 2023. DOI: 10.1007/s40964-023-00471-2. [Online]. Available: https://www.scopus.com/inward/record.uri?eid=2-s2.0-85163214782&doi=10.1007%2fs40964-023-00471-2&partnerID=40&md5=54a6f2545188535b7672e5c0172d6736.

[22] S. Bagherifard and M. Guagliano, *Post-processing*. 2021, pp. 327–348. DOI: 10.1016/B978-0-12-824090-8.00001-9. [Online]. Available: https://www.scopus.com/inward/record.uri?eid=2-s2.0-85122001577&doi=10.1016%2fB978-0-12-824090-8.00001-9&partnerID=40&md5=2d16785792c1340f840e36dd3ef80c4a.

[23] J. Metelkova, D. Ordnung, Y. Kinds, A. Witvrouw, and B. van Hooreweder, "Improving the quality of up-facing inclined surfaces in laser powder bed fusion of metals using a dual laser setup," vol. 94, 2020, pp. 266–269. DOI: 10.1016/j.procir.2020.09.050. [Online]. Available: https://www.scopus.com/inward/record.uri?eid=2-s2.0-85093364351&doi=10.1016%2fj.procir.2020.09.050&partnerID=40&md5=879fecee95ff6f34208895a71082aae6.

[24] Ö. Poyraz, E. U. Solakoğlu, S. Ören, C. Tüzemen, and G. Akbulut, "Surface texture and form characterization for powder bed additive manufacturing; [toz yatağı katmanlı imalat prosesinde yüzey dokusu ve form karakterizasyonu]," *Journal of the Faculty of Engineering and Architecture of Gazi University*, vol. 34, no. 3, pp. 1653–1664, 2019. DOI: 10.17341/gazimmfd.461588.

[Online]. Available: https://www.scopus.com/inward/record.uri?eid=2-s2.0-85069742882&doi=10.17341%2fgazimmfd.461588&partnerID=40&md5=e474db303c45f5697983b07e1e59d01e.

[25] C. Druzgalski, A. Ashby, G. Guss, W. King, T. Roehling, and M. Matthews, "Process optimization of complex geometries using feed forward control for laser powder bed fusion additive manufacturing," *Additive Manufacturing*, vol. 34, p. 101 169, 2020, ISSN: 2214-8604. DOI: https://doi.org/10.1016/j.addma.2020.101169. [Online]. Available: https://www.sciencedirect.com/science/article/pii/S2214860420305418.

[26] K. P. K. Reddy, B. N. Rao, M. Nazeemudheen, S. K. Manwatkar, and S. V. S. N. Murty, "Selection of optimal process parameters to obtain defect-free builds in in718 made by laser powder bed fusion," *Journal of Materials Engineering and Performance*, vol. 33, no. 19, pp. 10 228–10 241, 2024. DOI: 10.1007/s11665-023-08677-9. [Online]. Available: https://www.scopus.com/inward/record.uri?eid=2-s2.0-85170074292&doi=10.1007%2fs11665-023-08677-9&partnerID=40&md5=a4573142594b85e5adba05401f0c1403.

[27] M. Matthews, T. Roehling, S. Khairallah, *et al.*, "Controlling melt pool shape, microstructure and residual stress in additively manufactured metals using modified laser beam profiles," vol. 94, 2020, pp. 200–204. DOI: 10.1016/j.procir.2020.09.038. [Online]. Available: https://www.scopus.com/inward/record.uri?eid=2-s2.0-85093364516&doi=10.1016%2fj.procir.2020.09.038&partnerID=40&md5=ecfeb582e384e8aaffd2e24d56731de6.

[28] W. Wang, Y. Zhang, C. Yue, *et al.*, "Processing defect, microstructure evolution and mechanical properties of laser powder bed fusion al-12si alloys," *Journal of Materials Research and Technology*, vol. 26, pp. 681–696, 2023. DOI: 10.1016/j.jmrt.2023.07.231. [Online]. Available: https://www.scopus.com/inward/record.uri?eid=2-s2.0-85169539097&doi=10.1016%2fj.jmrt.2023.07.231&partnerID=40&md5=5145635cc62afef3e806c23847ab37a2.

[29] U. P. Singh, A. Shukla, S. Swaminathan, and G. Phanikumar, "Effect of build orientations on residual stress, microstructure, and mechanical properties of additively manufactured alloy-718 components," *Journal of Manufacturing Processes*, vol. 113, pp. 1–15, 2024. DOI: 10.1016/j.jmapro.2024.01.047. [Online]. Available: https://www.scopus.com/inward/record.uri?eid=2-s2.0-85185162370&doi=10.1016%2fj.jmapro.2024.01.047&partnerID=40&md5=172aa99d51f2a3ba12210b8772d92e14.

[30] L. Zhang, J. Lifton, Z. Hu, R. Hong, and S. Feih, "Influence of geometric defects on the compression behaviour of thin shell lattices fabricated by micro laser powder bed fusion," *Additive Manufacturing*, vol. 58, 2022. DOI: 10.1016/j.addma.2022.103038. [Online]. Available: https://www.scopus.com/inward/record.uri?eid=2-s2.0-85134684249&doi=10.1016%2fj.addma.2022.103038&partnerID=40&md5=40f7f95008fb4b235d07c5a644ed4e31.

[31] A. Ashby, G. Guss, R. K. Ganeriwala, *et al.*, "Thermal history and high-speed optical imaging of overhang structures during laser powder bed fusion: A computational and experimental analysis," *Additive Manufacturing*, vol. 53, 2022. DOI: 10.1016/j.addma.2022.102669. [Online]. Available: https://www.scopus.com/inward/record.uri?eid=2-s2.0-85125525777&doi=10.1016%2fj.addma.2022.102669&partnerID=40&md5=3edf78b43fa167adcc3b49c9e7e93044.

[32] A. Carrozza, B. Bircher, A. Aversa, *et al.*, "Investigating complex geometrical features in lpbf-produced parts: A material-based comparison between different titanium alloys," *Metals and Materials International*, vol. 29, pp. 3697–3714, 2023. DOI: 10.1007/s12540-023-01460-4. [Online]. Available: https://link.springer.com/article/10.1007/s12540-023-01460-4#Abs1.

[33] G. Yang, H. Li, Z. Li, *et al.*, "Support design of overhanging structure for laser powder bed fusion," *Journal of Materials Research and Technology*, vol. 24, pp. 8693–8702, 2023, ISSN: 2238-7854. DOI: https://doi.org/10.1016/j.jmrt.2023.05.087. [Online]. Available: https://www.sciencedirect.com/science/article/pii/S2238785423010566.

[34] P. Lin, M. Wang, V. A. Trofimov, Y. Yang, and C. Song, "Research on the warping and dross formation of an overhang structure manufactured by laser powder bed fusion," *Applied Sciences (Switzerland)*, vol. 13, no. 6, 2023. DOI: 10.3390/app13063460. [Online]. Available: https://www.scopus.com/inward/record.uri?eid=2-s2.0-85152040220&doi=10.3390%2fapp13063460&partnerID=40&md5=787e410635bea85ff438a02778ab71b3.

[35] M. Khorasani, M. Leary, D. Downing, *et al.*, "Numerical and experimental investigations on manufacturability of al–si–10mg thin wall structures made by lb-pbf," *Thin-Walled Structures*, vol. 188, 2023, Cited by: 11; All Open Access, Green Open Access. DOI: 10.1016/j.tws.2023.110814. [Online]. Available: https://www.scopus.com/inward/record.uri?eid=2-s2.0-85160798165&doi=10.1016%2fj.tws.2023.110814&partnerID=40&md5=cdcdb5e9632079ad54a6ce882476df97.

[36] X. Zhu, A. Dong, L. Cheng, J. Sun, Z. Liu, and L. Guo, "Study on alsi10mg alloy with complex flow channels by laser powder bed fusion," *Laser and Optoelectronics Progress*, vol. 60, no. 7, 2023. DOI: 10.3788/LOP220455. [Online]. Available: https://www.scopus.com/inward/record.uri?eid=2-s2.0-85166927749&doi=10.3788%2fLOP220455&partnerID=40&md5=919db394ffae8e72585cc793e16638a8.

[37] X. Chen, H. Wei, T. Liu, *et al.*, "In-situ monitoring and diagnostics for deposition defects in laser powder bed fusion process based on optical signals of melt pool," *Zhongguo Jiguang/Chinese Journal of Lasers*, vol. 51, no. 10, 2024. DOI: 10.3788/CJL240472. [Online]. Available: https://www.scopus.com/inward/record.uri?eid=2-s2.0-85193061627&doi=10.3788%2fCJL240472&partnerID=40&md5=77b427ca17c478124c477da3f439af77.

[38] B. Whip, L. Sheridan, and J. Gockel, "The effect of primary processing parameters on surface roughness in laser powder bed additive manufacturing," *International Journal of Advanced Manufacturing Technology*, vol. 103, no. 9-12, pp. 4411–4422, 2019. DOI: 10.1007/s00170-019-03716-z. [Online]. Available: https://www.scopus.com/inward/record.uri?eid=2-s2.0-85066868490&doi=10.1007%2fs00170-019-03716-z&partnerID=40&md5=0f7ec8a22676c5fb1c8b1804897798bb.

[39] M. Leary, M. Khorasani, A. Sarker, *et al.*, "7 - surface roughness," in *Fundamentals of Laser Powder Bed Fusion of Metals*, ser. Additive Manufacturing Materials and Technologies, I. Yadroitsev, I. Yadroitsava, A. du Plessis, and E. MacDonald, Eds., Elsevier, 2021, pp. 179–213, ISBN: 978-0-12-824090-8. DOI: https://doi.org/10.1016/B978-0-12-824090-8.00023-8. [Online]. Available: https://www.sciencedirect.com/science/article/pii/B9780128240908000238.

[40] X. He, B. Yang, D. Kong, *et al.*, "An integrated multiscale simulation guiding the processing optimisation for additively manufactured nickel-based superalloys," *Virtual and Physical Prototyping*, vol. 19, no. 1, 2024. DOI: 10.1080/17452759.2024.2313661. [Online]. Available: https://www.scopus.com/inward/record.uri?eid=2-s2.0-85184661564&doi=10.1080%2f17452759.2024.2313661&partnerID=40&md5=91bf8312a63a3e008b0a5321686ac33e.

[41] H. Hayashi, S. Tokita, Y. S. Sato, *et al.*, "Microstructure and mechanical property of laser powder bed fusion additive manufactured al-10si-mg alloy," *Keikinzoku Yosetsu/Journal of Light Metal Welding*, vol. 62, no. 12, pp. 581–586, 2024. DOI: 10.11283/jlwa.62.581. [Online]. Available: https://www.scopus.com/inward/record.uri?eid=2-s2.0-85213453677&doi=10.11283%2fjlwa.62.581&partnerID=40&md5=be8d8265a1176a64df17edb5c21d6fed.

[42] M. Palm, B. Diepold, S. Neumeier, H. Hoeppel, M. Goeken, and M. Zaeh, "Detection and effects of lack of fusion defects in hastelloy x manufactured by laser powder bed fusion," *Materials Design*, vol. 230, p. 111 941, 2023, ISSN: 0264-1275. DOI: https://doi.org/10.1016/j.matdes.2023.111941. [Online]. Available: https://www.sciencedirect.com/science/article/pii/S0264127523003568.

[43] C. Porter, F. M. Carter, D. Kozjek, *et al.*, "Qualitative analysis of potential pore healing phenomenon in l-pbf using operando high speed x-ray imaging," *Manufacturing Letters*, vol. 35, pp. 636–642, 2023, 51st SME North American Manufacturing Research Conference (NAMRC 51), ISSN: 2213-8463. DOI: https://doi.org/10.1016/j.mfglet.2023.08.052. [Online]. Available: https://www.sciencedirect.com/science/article/pii/S2213846323001098.

[44] S. Shrestha and K. Chou, "Formation of keyhole and lack of fusion pores during the laser powder bed fusion process," *Manufacturing Letters*, vol. 32, pp. 19–23, 2022. DOI: 10.1016/j.mfglet.2022.01.005. [Online]. Available: https://www.scopus.com/inward/record.uri?eid=2-s2.0-85124303056&doi=10.1016%2fj.mfglet.2022.01.005&partnerID=40&md5=18cdd97fcb45eae43b30f49fbe443343.

[45] C. Zhao, N. D. Parab, X. Li, *et al.*, "Critical instability at moving keyhole tip generates porosity in laser melting," *Science*, vol. 370, no. 6520, pp. 1080–1086, 2020. DOI: 10.1126/science.abd1587. [Online]. Available: https://www.science.org/doi/abs/10.1126/science.abd1587.

[46] S. Ly, A. M., S. A. Rubenchik, Khairallah, G. Guss, and M. J. Matthews1, "Metal vapor micro-jet controls material redistribution in laser powder bed fusion additive manufacturing," *Scientific Reports*, vol. 7, p. 4085, Jun. 2017. DOI: 10.1038/s41598-017-04237-z.

[47] Z. Li, H. Li, J. Yin, *et al.*, "A review of spatter in laser powder bed fusion additive manufacturing: In situ detection, generation, effects, and countermeasures," *Micromachines*, vol. 13, no. 8, 2022, ISSN: 2072-666X. DOI: 10.3390/mi13081366. [Online]. Available: https://www.mdpi.com/2072-666X/13/8/1366.

[48] A. Philo, D. Butcher, S. Sillars, *et al.*, "A multiphase cfd model for the prediction of particulate accumulation in a laser powder bed fusion process," *Minerals, Metals and Materials Series*, vol. Part F3, pp. 65–76, 2018. DOI: 10.1007/978-3-319-72059-3_7. [Online]. Available: https://www.scopus.com/inward/record.uri?eid=2-s2.0-85042294676&doi=10.1007%2f978-3-319-72059-3_7&partnerID=40&md5=012dece52f260e4cbf901d000f2b7431.

[49] A. Gasper, B. Szost, X. Wang, *et al.*, "Spatter and oxide formation in laser powder bed fusion of inconel 718," *Additive Manufacturing*, vol. 24, pp. 446–456, 2018. DOI: 10.1016/j.addma.2018.09.032. [Online]. Available: https://www.scopus.com/inward/record.uri?eid=2-s2.0-85055553876&doi=10.1016%2fj.addma.2018.09.032&partnerID=40&md5=4d407e9df7ba430678fe34a8308fd3

[50] Z. Li, H. Li, J. Yin, *et al.*, "A review of spatter in laser powder bed fusion additive manufacturing: In situ detection, generation, effects, and countermeasures," *Micromachines*, vol. 13, no. 8, 2022. DOI: 10.3390/mi13081366. [Online]. Available: https://www.scopus.com/inward/record.uri?eid=2-s2.0-85137603663&doi=10.3390%2fmi13081366&partnerID=40&md5=451c2397c3246d17a1c90a36d2fa16ac.

[51] D. Wang, Y. Ou, W. Dou, Y. Yang, and C. Tan, "Research progress on spatter behavior in laser powder bed fusion," *Zhongguo Jiguang/Chinese Journal of Lasers*, vol. 47, no. 9, 2020. DOI: 10.3788/CJL202047.0900001. [Online]. Available: https://www.scopus.com/inward/record.uri?eid=2-s2.0-85096166721&doi=10.3788%2fCJL202047.0900001&partnerID=40&md5=47f8893adff215375ac89136dca08c25.

[52] J. H. Yu, Q.-Y. Jin, K. Ha, and W. Lee, "Influence of several heat treatments on residual stress in laser powder bed-fused maraging 18ni-300 steel," *Applied Sciences*, vol. 13, no. 11, 2023, ISSN: 2076-3417. [Online]. Available: https://www.mdpi.com/2076-3417/13/11/6572.

[53] T. Machirori, F. Liu, Q. Yin, and H. Wei, "Spatiotemporal variations of residual stresses during multi-track and multi-layer deposition for laser powder bed fusion of ti-6al-4v," *Computational Materials Science*, vol. 195, p. 110 462, 2021, ISSN: 0927-0256. DOI: https://doi.org/10.1016/j.commatsci.2021.110462. [Online]. Available: https://www.sciencedirect.com/science/article/pii/S0927025621001877.

[54] A. Ghasemi, R. A. Yildiz, and M. Malekan, "Investigating temperature, stress, and residual stresses in laser powder bed fusion additive manufacturing of inconel 625," *Materials Today Communications*, vol. 41, p. 110 694, 2024, ISSN: 2352-4928. DOI: https://doi.org/10.1016/j.mtcomm.2024.110694. [Online]. Available: https://www.sciencedirect.com/science/article/pii/S2352492824026758.

[55] E. Lanigan, "Insitu process monitoring a perspective on the role of in situ process monitoring in the certification of additive manufactured space hardware," *Materials Evaluation*, vol. 80, no. 4, pp. 24–27, 2022, Cited by: 0. DOI: 10.32548/2022.me-04261. [Online]. Available: https://www.scopus.com/inward/record.uri?eid=2-s2.0-85159076468&doi=10.32548%2f2022.me-04261&partnerID=40&md5=202d74dd53d4c4101c1139a84782af3b.

[56] R. McCann, M. A. Obeidi, C. Hughes, *et al.*, "In-situ sensing, process monitoring and machine control in laser powder bed fusion: A review," *Additive Manufacturing*, vol. 45, p. 102 058, 2021, ISSN: 2214-8604. DOI: https://doi.org/10.1016/j.addma.2021.102058. [Online]. Available: https://www.sciencedirect.com/science/article/pii/S2214860421002232.

[57] M. G. Guerra, V. Errico, A. Fusco, F. Lavecchia, S. L. Campanelli, and L. M. Galantucci, "High resolution-optical tomography for in-process layer-wise monitoring of a laser-powder bed fusion technology," *Additive Manufacturing*, vol. 55, p. 102 850, 2022, ISSN: 2214-8604. DOI: https://doi.org/10.1016/j.addma.2022.102850. [Online]. Available: https://www.sciencedirect.com/science/article/pii/S2214860422002494.

[58] O. Ero, K. Taherkhani, and E. Toyserkani, "Optical tomography and machine learning for in-situ defects detection in laser powder bed fusion: A self-organizing map and u-net based approach," *Additive Manufacturing*, vol. 78, p. 103 894, 2023, ISSN: 2214-8604. DOI: https://doi.org/10.1016/j.addma.2023.103894. [Online]. Available: https://www.sciencedirect.com/science/article/pii/S2214860423005079.

[59] C. Schwerz and L. Nyborg, "Pixel intensity of near-infrared long-exposure images acquired in-situ as a quality control tool in laser powder bed fusion of ni-base hastelloy x," 2022. [Online]. Available: https://www.scopus.com/inward/record.uri?eid=2-s2.0-85160791098&partnerID=40&md5=4303ef7034ae80b539574804395226c3.

[60] European Environment Agency. "Ex-situ." (n.d.), [Online]. Available: https://www.eea.europa.eu/help/glossary/chm-biodiversity/ex-situ.

[61] W. A. Kalender, "X-ray computed tomography," *Physics in Medicine & Biology*, vol. 51, no. 13, R29, Jun. 2006. DOI: 10.1088/0031-9155/51/13/R03. [Online]. Available: https://dx.doi.org/10.1088/0031-9155/51/13/R03.

[62] R. Chityala, *X-ray and computed tomography*. 2010, 26–1 – 26–13, Cited by: 0. DOI: 10.1201/9781420075250. [Online]. Available: https://www.scopus.com/inward/record.uri?eid=2-s2.0-85055804881&doi=10.1201%2f9781420075250&partnerID=40&md5=250b6593eee6caa931ddf39a6a571b00.

[63] W. Sun, C. Giusca, S. Lou, *et al.*, "Establishment of x-ray computed tomography traceability for additively manufactured surface texture evaluation," *Additive Manufacturing*, vol. 50, p. 102 558, 2022, ISSN: 2214-8604. DOI: https://doi.org/10.1016/j.addma.2021.102558. [Online]. Available: https://www.sciencedirect.com/science/article/pii/S2214860421007053.

[64] R. M. Reilly, *X-ray, CT, and mammography technology*. 2019, pp. 11–26, Cited by: 0. DOI: 10.1002/9781119537397.ch2. [Online]. Available: https://www.scopus.com/inward/record.uri?eid=2-s2.0-85102158662&doi=10.1002%2f9781119537397.ch2&partnerID=40&md5=9b860625d5380b095050103cedb8d0bb

[65] E. Dach, B. Bergauer, A. Seidel, *et al.*, "Impact of voxel size and scan time on the accuracy of three-dimensional radiological imaging data from cone-beam computed tomography," *Journal of Cranio-Maxillofacial Surgery*, vol. 46, no. 12, pp. 2190–2196, 2018, Cited by: 12. DOI: 10.1016/j.jcms.2018.09.002. [Online]. Available: https://www.scopus.com/inward/record.uri?eid=2-s2.0-85054563034&doi=10.1016%2fj.jcms.2018.09.002&partnerID=40&md5=e742a9c012e5acc89dcbd5b4de8df284.

[66] W. Technologies, *Phoenix v|tome|x m microfocus ct manual*, BHFF31319EN_2023-01_Phoenix-Vtomex-M_A4_V02, Waygate Technologies, Jan. 2023. [Online]. Available: https://waygate-tech.com.

[67] W. Technologies, *Phoenix datos|x industrial ct acquisition & reconstruction software*, Accessed: 2025-04-29, 2025. [Online]. Available: https://www.bakerhughes.com/waygate-technologies/ndt-software/phoenix-datosx-industrial-ct-acquisition-reconstruction-software.

[68] *Vgstudio max*, Accessed: 2025-03-26, 2025. [Online]. Available: https://www.volumegraphics.com/en/products/vgstudio-max.html.

[69] J. Satoh, *Product review: Vgstudio by volume graphics*, 2022. [Online]. Available: https://www.rigaku.com/en/products/vgstudio-max.html.

[70] S. Bergmueller, L. Gerhold, L. Fuchs, L. Kaserer, and G. Leichtfried, "Systematic approach to process parameter optimization for laser powder bed fusion of low-alloy steel based on melting modes," *International Journal of Advanced Manufacturing Technology*, vol. 126, no. 9-10, pp. 4385–4398, 2023, Cited by: 10; All Open Access, Hybrid Gold Open Access. DOI: 10.1007/s00170-023-11377-2. [Online]. Available: https://www.scopus.com/inward/record.uri?eid=2-s2.0-85153057907&doi=10.1007%2fs00170-023-11377-2&partnerID=40&md5=56b9622e7d36d1734ccd6911d6ca93db.

[71] C. Schwerz, B. A. Bircher, A. Küng, and L. Nyborg, "In-situ detection of stochastic spatter-driven lack of fusion: Application of optical tomography and validation via ex-situ x-ray computed tomography," *Additive Manufacturing*, vol. 72, p. 103 631, 2023, ISSN: 2214-8604. DOI: https://doi.org/10.1016/j.addma.2023.103631. [Online]. Available: https://www.sciencedirect.com/science/article/pii/S2214860423002440.

[72] H. Kong, H. C. Akakin, and S. E. Sarma, "A generalized laplacian of gaussian filter for blob detection and its applications," *IEEE Transactions on Cybernetics*, vol. 43, no. 6, pp. 1719–1733, 2013. DOI: 10.1109/TSMCB.2012.2228639.

[73] G. Yu, K. Yoon, S. Lee, Y. Shin, and J. Park, "Distortion measurement metric for human image refinement and evaluation using distorted image datasets," *IEEE Access*, vol. 13, pp. 34 390–34 408, 2025. DOI: 10.1109/ACCESS.2025.3543542.

[74] M. Cantone, C. Marrocco, F. Tortorella, and A. Bria, "Learnable dog convolutional filters for microcalcification detection," *Artificial Intelligence in Medicine*, vol. 143, 2023, Cited by: 2. DOI: 10.1016/j.artmed.2023.102629. [Online]. Available: https://www.scopus.com/inward/record.uri?eid=2-s2.0-85166299599&doi=10.1016%2fj.artmed.2023.102629&partnerID=40&md5=d6bc6398e44bf89f4737fe79c9e872b2.

[75] L. Wang and Y. Sun, "Improved canny edge detection algorithm," Cited by: 6, 2021, pp. 414–417. DOI: 10.1109/ICCSMT54525.2021.00081. [Online]. Available: https://www.scopus.com/inward/record.uri?eid=2-s2.0-85133259115&doi=10.1109%2fICCSMT54525.2021.00081&partnerID=40&md5=377c3a34f292fdc7ba83a26afc09dc9c.

[76] I. Sunit Rout, P. Pandian, and A. Raj, "Variable parametric test to improve the machinability of inconel-718 using tungsten carbide tool," *Materials Today: Proceedings*, vol. 47, pp. 5564–5569, 2021, 3rd International e-Conference on Frontiers in Mechanical Engineering and nanoTechnology, ISSN: 2214-7853. DOI: https://doi.org/10.1016/j.matpr.2021.03.456. [Online]. Available: https://www.sciencedirect.com/science/article/pii/S2214785321025116.

[77] J. Belan, L. Hurtalova, A. Vasko, and E. Tillova, "Metallography evaluation of in 718 after applied heat treatment", journal="manufacturing technology journal," vol. 14, no. 3, pp. 262–267, 2014, ISSN: 12132489. DOI: 10.21062/ujep/x.2014/a/1213-2489/MT/14/3/262. [Online]. Available: https://doi.org/10.21062/ujep/x.2014/a/1213-2489/MT/14/3/262.

[78] E. Hosseini and V. Popovich, "A review of mechanical properties of additively manufactured inconel 718," *Additive Manufacturing*, vol. 30, 2019. DOI: 10.1016/j.addma.2019.100877. [Online]. Available: https://www.scopus.com/inward/record.uri?eid=2-s2.0-85072709387&doi=10.1016%2fj.addma.2019.100877&partnerID=40&md5=552484f1917b62e0a2c042b115e64d31.

[79] K. M. Döleker, A. Erdogan, T. Yener, *et al.*, "Enhancing the wear and oxidation behaviors of the inconel 718 by low temperature aluminizing," *Surface and Coatings Technology*, vol. 412, p. 127 069, 2021, ISSN: 0257-8972. DOI: https://doi.org/10.1016/j.surfcoat.2021.127069. [Online]. Available: https://www.sciencedirect.com/science/article/pii/S0257897221002437.

[80] A. Shokrani, V. Dhokia, and S. T. Newman, "Hybrid cooling and lubricating technology for cnc milling of inconel 718 nickel alloy," vol. 11, 2017, pp. 625–632. DOI: 10.1016/j.promfg.2017.07.160. [Online]. Available: https://www.scopus.com/inward/record.uri?eid=2-s2.0-85029854258&doi=10.1016%2fj.promfg.2017.07.160&partnerID=40&md5=87dcac0d416aa65db6c6f3693d149e32.

[81] M. Montazeri, A. R. Nassar, A. J. Dunbar, and P. Rao, "In-process monitoring of porosity in additive manufacturing using optical emission spectroscopy," *IISE Transactions*, vol. 52, no. 5, pp. 500–515, 2020. DOI: 10.1080/24725854.2019.1659525. [Online]. Available: https://www.scopus.com/inward/record.uri?eid=2-s2.0-85074033501&doi=10.1080%2f24725854.2019.1659525&partnerID=40&md5=a70219c6cc854484b2d2cc0556b5ef8c.

[82] R. Rakshit and A. K. Das, "A review on cutting of industrial ceramic materials," *Precision Engineering*, vol. 59, pp. 90–109, 2019, ISSN: 0141-6359. DOI: https://doi.org/10.1016/j.precisioneng.2019.05.009. [Online]. Available: https://www.sciencedirect.com/science/article/pii/S0141635919300224.

[83] Z. Huang, G. Li, S. Tian, X. Song, M. Sheng, and S. Shah, "Chapter one - theoretical basis of abrasive jet," in *Abrasive Water Jet Perforation and Multi-Stage Fracturing*, Z. Huang, G. Li, S. Tian, X. Song, M. Sheng, and S. Shah, Eds., Gulf Professional Publishing, 2018, pp. 1–62, ISBN: 978-0-12-812807-7. DOI: https://doi.org/10.1016/B978-0-12-812807-7.00001-7. [Online]. Available: https://www.sciencedirect.com/science/article/pii/B9780128128077000017.

[84] M. Guide. "3d abrasive water jet cutting of flat materials." Accessed: 2025-03-24. (2025), [Online]. Available: https://www.manufacturingguide.com/en/3d-abrasive-water-jet-cutting-flat-materials.

[85] Jagadish and K. Gupta, "Introduction to abrasive water jet machining," in *Abrasive Water Jet Machining of Engineering Materials*. Cham: Springer International Publishing, 2020, pp. 1–11, ISBN: 978-3-030-36001-6. DOI: 10.1007/978-3-030-36001-6_1. [Online]. Available: https://doi.org/10.1007/978-3-030-36001-6_1.

[86] Y. Jia, B. S. Kim, D. J. Hu, and J. Ni, "Parametric study on near-dry wire electrodischarge machining of polycrystalline diamond-coated tungsten carbide material," *Proceedings of the Institution of Mechanical Engineers, Part B*, vol. 224, no. 2, pp. 185–193, 2010. DOI: 10.1243/09544054JEM1602. [Online]. Available: https://doi.org/10.1243/09544054JEM1602.

[87] R. D. Khatu, B. T. Patil, D. K. Bhise, and H. B. Vaishnav, "Design of a fixture for wire-cut edm: A generic approach," *Materials Today: Proceedings*, vol. 49, pp. 2034–2041, 2022, GC-RASM 2021, ISSN: 2214-7853. DOI: https://doi.org/10.1016/j.matpr.2021.08.214. [Online]. Available: https://www.sciencedirect.com/science/article/pii/S2214785321056522.

[88] S. R. Dhale and B. B. Deshmukh, "Investigations into the effect of varying electrode diameter on cutting rate and kerf width in wedm of varying thickness inconel718," *Lecture Notes on Multidisciplinary Industrial Engineering*, vol. Part F165, pp. 571–582, 2020. DOI: 10.1007/978-981-32-9471-4_47. [Online]. Available: https://www.scopus.com/inward/record.uri?eid=2-s2.0-85138187441&doi=10.1007%2f978-981-32-9471-4_47&partnerID=40&md5=57018f924472e388e56a75e911e96e86.

[89] P. Pitayachaval, P. Jittamai, and T. Baothong, "A review of machining parameters that effect to wire electrode wear," 2017, pp. 1–4. DOI: 10.1109/IEA.2017.7939167. [Online]. Available: https://www.scopus.com/inward/record.uri?eid=2-s2.0-85021449167&doi=10.1109%2fIEA.2017.7939167&partnerID=40&md5=6f8adbc30b8b785ec5aabd72f651a11c.

[90] UnionFab. "Wire edm." (2023), [Online]. Available: https://www.unionfab.com/blog/2023/10/wire-edm.

[91] M. Javaid, A. Haleem, R. Pratap Singh, and R. Suman, "Industrial perspectives of 3d scanning: Features, roles and it's analytical applications," *Sensors International*, vol. 2, 2021, Cited by: 84; All Open Access, Gold Open Access. DOI: 10.1016/j.sintl.2021.100114. [Online]. Available: https://www.scopus.com/inward/record.uri?eid=2-s2.0-85119017364&doi=10.1016%2fj.sintl.2021.100114&partnerID=40&md5=7bd2e58ffc9b56a11a164c0e6928ce90.

[92] A. Haleem, M. Javaid, R. P. Singh, *et al.*, "Exploring the potential of 3d scanning in industry 4.0: An overview," *International Journal of Cognitive Computing in Engineering*, vol. 3, pp. 161–171, 2022, Cited by: 53; All Open Access, Gold Open Access. DOI: 10.1016/j.ijcce.2022.08.003. [Online]. Available: https://www.scopus.com/inward/record.uri?eid=2-s2.0-85146000211&doi=10.1016%2fj.ijcce.2022.08.003&partnerID=40&md5=e1a14b91dd4ec6aef143bc3565c4e4ae.

[93] *Metrology: Gom atos scanbox 6130*, https://search.rsc.a-star.edu.sg/equipment/metrology-gom-atos-scanbox-6130-artc, Accessed: 2025-05-20.

[94] *Zeiss inspect: One metrology software*, https://www.zeiss.com/metrology/en/software/zeiss-inspect.html, Accessed: 2025-05-20.

[95] J. V. Gordon, S. P. Narra, R. W. Cunningham, *et al.*, "Defect structure process maps for laser powder bed fusion additive manufacturing," *Additive Manufacturing*, vol. 36, p. 101 552, 2020, ISSN: 2214-8604. DOI: https://doi.org/10.1016/j.addma.2020.101552. [Online]. Available: https://www.sciencedirect.com/science/article/pii/S2214860420309246.

[96] E. GmbH. "Eos m 290 - metal 3d printer." Accessed: 2025-03-05. (2025), [Online]. Available: https://www.eos.info/metal-solutions/metal-printers/eos-m-290#technical-data.

[97] C. Pauzon, A. Raza, I. Hanif, S. Dubiez-Le Goff, J. Moverare, and E. Hryha, "Effect of layer thickness on spatter properties during laser powder bed fusion of ti–6al–4v," *Powder Metallurgy*, vol. 66, no. 4, pp. 333–342, 2023. DOI: 10.1080/00325899.2023.2192036. [Online]. Available: https://www.scopus.com/inward/record.uri?eid=2-s2.0-85151087958&doi=10.1080%2f00325899.2023.2192036&partnerID=40&md5=8fe6ed8511baeb6e79640800f2bbb822.

[98] E. GmbH. "3d printing software for monitoring and quality assurance." Accessed: 2025-03-11. (2025), [Online]. Available: https://uk.eos.info/en/industrial-3d-printer/software/monitoring.

[99] G. Chebil, P. Lapouge, Y. Renollet, *et al.*, "Study of spatter ejections during laser-powder bed fusion process for aluminum alloys," *Journal of Laser Applications*, vol. 33, no. 4, 2021, Cited by: 2; All Open Access, Green Open Access. DOI: 10.2351/7.0000493. [Online]. Available: https://www.scopus.com/inward/record.uri?eid=2-s2.0-85118952275&doi=10.2351%2f7.0000493&partnerID=40&md5=3f25fa73e2b5fdf423a5cc86e5ca3451.

[100] Z. Tao, A. Thanki, L. Goossens, A. Witvrouw, B. Vrancken, and W. Dewulf, "Data-driven keyhole pore detection in laser powder bed fusion: Integrating process insights with x-ct," *Journal of Manufacturing Processes*, vol. 142, pp. 293–316, 2025. DOI: 10.1016/j.jmapro.2025.03.107. [Online]. Available: https://www.scopus.com/inward/record.uri?eid=2-s2.0-105001496407&doi=10.1016%2fj.jmapro.2025.03.107&partnerID=40&md5=7176fd733372c140355533ca9203934f.

Department of Industrial- and Materials Science
CHALMERS TEKNISKA HÖGSKOLA
Göteborg, Sverige
www.chalmers.se

CHALMERS